The Mevalonate Pathway Drives Tumor Immune Evasion via RalB-Mediated PD-L1 Trafficking

Meng Hao[1], Jixing Zhong[1], Ying Huang[1], Bin Huang[1], Weiyao Kong[1], Yi Wang[1, 2, 3], Dan Luo[1], Yu Zhang[1, 4], Hui Wang[1, 2, 3], Yi Zhou[1,5], Ying He[1, 6], Juyuan Wang[1, 7], Yong Nian[8], Lei Zhang[1,2,4] and Chengqian Yin[1,2*]

1 Institute of Cancer Research, Shenzhen Bay Laboratory, Shenzhen, Guangdong, China.

2 Shenzhen Medical Academy of Research and Translation (SMART), Shenzhen, Guangdong, China.

3 School of Life Sciences, Westlake University, Hangzhou, Zhejiang, China.

4 School of Chemical Biology and Biotechnology, Peking University Shenzhen Graduate School, Shenzhen, Guangdong, China.

5 Department of Biochemistry, School of Medicine, Southern University of Science and Technology, Shenzhen, Guangdong, China.

6 School of Medicine and Health, Harbin Institute of Technology, Harbin, China.

7 Hong Kong University of Science and Technology, Hong Kong, China.

8 College of Pharmacy, Nanjing Drum Tower Hospital, Nanjing University of Chinese Medicine, Nanjing, Jiangsu, China.

*Corresponding author: Chengqian Yin (yincq@szbl.ac.cn).

Abstract

Tumor metabolic rewiring supports malignant growth and can concurrently dampen antitumor immunity, yet how the tumor-intrinsic mevalonate (MVA) pathway enforces immune escape remains insufficiently defined. Here we show that genetic or pharmacologic disruption of the MVA pathway in tumor cells elicits a robust immune response, increasing intratumoral CD8$^+$ T cell infiltration and effector function and thereby constraining tumor growth. Mechanistically, we identify farnesyl pyrophosphate synthase (FDPS) as a central metabolic-immune node that modulates the isoprenoid pool, altering levels of geranylgeranyl pyrophosphate (GGPP) and consequently the geranylgeranylation status of the small GTPase RalB. RalB geranylgeranylation in turn exerts dual control of tumor cell PD-L1, promoting PD-L1 surface availability through regulation of protein trafficking while also augmenting PD-L1 expression at the transcriptional level. Therapeutically, inhibition of FDPS using clinically established nitrogen-containing bisphosphonates potentiates PD-1/CTLA-4 blockades and yields marked antitumor activity in vivo. Collectively, these findings define a tumor-intrinsic MVA-GGPP-RalB axis that drives PD-L1-dependent immune evasion and provide a mechanistic rationale for repurposing nitrogen-containing bisphosphonates as rational combinatorial agents to improve the efficacy of immune checkpoint blockade.

Highlights

1. Tumor-intrinsic mevalonate pathway inhibits CD8$^+$ T cell-mediated anti-tumor immunity
2. FDPS enhances PD-L1 transcription and promotes PD-L1 surface recycling via GGPP-dependent RalB geranylgeranylation
3. Nitrogenous bisphosphonates (N-BPs) enhance PD-1/CTLA-4 blockades in preclinical models
4. High FDPS expression is associated with reduced CD8+ T cell infiltration and poor prognosis

Introduction

The immune system can recognize and eliminate malignant cells, yet tumors have evolved multiple mechanisms to evade immune surveillance. Immune checkpoint blockade (ICB), prominently targeting PD-1/PD-L1 and CTLA-4, has reshaped cancer treatment by reinvigorating tumor-reactive T cells [1]. Despite ICB induces durable benefit in a subset of patients, many tumors remain poorly infiltrated by cytotoxic T cells and exhibit primary non-response or acquired resistance [2]. A central challenge is to define tumor-intrinsic programs that actively enforce an immunosuppressive tumor microenvironment and to identify actionable nodes that can convert ineffective immunity into productive antitumor T-cell responses.

Metabolic rewiring is increasingly recognized as a key determinant of immune exclusion and T-cell dysfunction within tumors [3]. The mevalonate (MVA) pathway has attracted growing attention for its tumor-promoting and immunoregulatory function as a central source of cholesterol and isoprenoid intermediates [4]. Clinically, pharmacologic inhibition of the MVA pathway with statins is widely used for cardiovascular risk reduction, and retrospective analyses have reported an association between statin treatment and improved outcomes in patients receiving immunotherapy [5-7]. These observations implicate the MVA pathway in tumor immune escape, but the relevant enzymatic nodes and the mechanistic links to immune checkpoint control remain insufficiently defined.

Here, we identify farnesyl pyrophosphate synthase (FDPS) as a tumor-intrinsic metabolic-immune node that promotes immune evasion. We show that FDPS maintains GGPP-dependent prenylation of the small GTPase RalB, thereby enforcing dual regulation of PD-L1 by upregulating PD-L1 transcription and promoting PD-L1 recycling to the tumor cell surface. Genetic or pharmacologic disruption of FDPS augments intratumoral CD8$^+$ T-cell infiltration and effector function, resulting in suppressed tumor growth. We further evaluate targeting FDPS with clinically established nitrogen-containing bisphosphonates as a rational strategy to potentiate PD-1/CTLA-4 blockades, providing a mechanistic framework for metabolism-directed enhancement of immunotherapy.

Results

Inhibition of the MVA pathway sensitizes tumor cells to CD8+ T cell-mediated cytotoxicity

To investigate the role of the mevalonate (MVA) pathway in tumor immune escape, we knocked down HMGCR and FDPS in B16F10 melanoma cells using shRNAs (Supplementary Fig. 1A, B). HMGCR and FDPS encode HMG-CoA reductase, the upstream rate-limiting enzyme, and farnesyl diphosphate synthase, a key downstream branch point in the MVA pathway. These enzymes are also clinically actionable targets, inhibited by statins for cardiovascular disease and by nitrogen-containing bisphosphonates for osteoporosis (Fig. 1A). In immunocompetent C57BL/6 mice, knockdown of either gene significantly attenuated tumor growth (Fig. 1B, C and Supplementary Fig. 1C, D). In contrast, in immunodeficient nude mice, the growth-inhibitory effect of HMGCR knockdown was markedly reduced and the effect of FDPS knockdown was completely lost (Fig. 1D, E and Supplementary Fig. 1E, F), indicating that the antitumor effects of MVA pathway disruption are largely immune dependent.

Analysis of tumor-infiltrating immune cells on day 14 revealed a significant increase in intratumoral CD8$^+$ T cells following HMGCR or FDPS knockdown (Fig. 1F and Supplementary Fig. 1G, H). Notably, FDPS knockdown enhanced CD8$^+$ T cell effector function, as indicated by elevated IFN-γ and granzyme B (GZMB) expression (Fig. 1G, H). Consistently, depletion of CD8$^+$ T cells significantly blunted the antitumor effect of FDPS knockdown (Fig. 1I, J and Supplementary Fig. 1I), establishing CD8$^+$ T cells as a principal mediator. Together, these data suggest that the MVA pathway, with FDPS as a key node, promotes immune escape by limiting CD8$^+$ T cell infiltration and cytotoxic activity.

To test whether MVA pathway disruption directly sensitizes tumor cells to CD8$^+$ T cell killing, we cocultured B16F10-OVA-GFP and MC38-OVA-GFP cells with $CD8^+$ T cells isolated from OT-1 mice. Consistent with our in vivo observations, knockdown of HMGCR or FDPS in tumor cells significantly increased OT-1 cytotoxicity, while having no significant effect on tumor cell viability in monoculture (Fig. 1K, L and Supplementary Fig. 1J, K). Pharmacologic inhibition of the MVA pathway using statins or bisphosphonates similarly sensitized tumor cells to $CD8^+$ T cell-mediated growth inhibition, while exerting minimal direct growth inhibition in tumor cells (Fig. 1M, N). Using a pretreatment design, we found that these inhibitors act primarily on tumor cells rather than directly on T cells to enhance $CD8^+$ T cell cytotoxicity (Fig. 1O, P). Moreover, the effect of pharmacologic inhibition was occluded in FDPS-knockdown cells, supporting FDPS as a key functional target (Supplementary Fig. 1L).

Given its pronounced immunomodulatory phenotype, we focused subsequent experiments on FDPS. In a lung metastasis model, FDPS knockdown reduced metastatic colonization (Fig. 1Q). In tumor rechallenge experiments, mice initially inoculated with FDPS-knockdown cells developed protective immune memory that suppressed subsequent control tumor growth and prolonged survival (Fig. 1R-T). Collectively, these results identify FDPS as a critical MVA pathway node that enables tumor immune escape by restraining $CD8^+$ T cell cytotoxicity, facilitating metastatic outgrowth, and limiting durable antitumor immune memory.

The GGPP-dependent geranylgeranylation regulates PD-L1 surface localization on tumor cells to control $CD8^+$ T cells function

Cholesterol, farnesyl diphosphate (FPP), and geranylgeranyl diphosphate (GGPP) are major downstream products of the MVA pathway regulated by FDPS. Accordingly, FDPS knockdown reduced intracellular levels of FPP, GGPP, and cholesterol (Supplementary Fig. 2A-C). Supplementation with these metabolites effectively reversed the enhanced $CD8^+$ T cell-mediated cytotoxicity observed upon FDPS knockdown (Fig. 2A, B). Then we separately pretreated tumor cells and $CD8^+$ T cells with each metabolite. Cholesterol primarily acted on T cells to diminish tumor-killing capacity, consistent with prior report linking cholesterol accumulation to $CD8^+$ T cell exhaustion [8]. In contrast, FPP and GGPP restored resistance to $CD8^+$ T cell cytotoxicity by acting on tumor cells (Fig. 2C, D). This observation prompted us to define the tumor-intrinsic changes driving this immunomodulatory effect. In the MVA pathway, FPP is a key branch point that is either converted to cholesterol via squalene synthase (SQS, encoded by Fdft1) or elongated to geranylgeranyl pyrophosphate (GGPP) by GGPPS. FPP and GGPP then serve as substrates for protein prenylation, including farnesylation by farnesyltransferase (FTase, encoded by Fntb) and geranylgeranylation by geranylgeranyltransferase (GGTase, encoded by Pggt1b) (Fig. 2E). We next interrogated distinct FPP-derived branches by knocking down Fdft1 (squalene synthesis), Fntb (farnesylation), or Pggt1b (geranylgeranylation) in tumor cells (Supplementary Fig. 2D-F). Consistent with the cholesterol supplementation experiments, Fdft1 knockdown did not affect $CD8^+$ T cell killing (Supplementary Fig. 2G). While Fntb knockdown did not change in $CD8^+$ T cell cytotoxicity, Pggt1b knockdown alone significantly potentiated $CD8^+$ T cell-mediated tumor killing (Fig. 2F). Concordantly, pharmacologic inhibition of GGTase with GGTi-298 markedly enhanced $CD8^+$

T cell cytotoxicity, whereas the FTase inhibitor tipifarnib produced no significant effect (Fig. 2G). Together, these data identify GGPP-dependent geranylgeranylation as the dominant FPP-derived branch limiting tumor susceptibility to CD8$^+$ T cell-mediated cytotoxicity.

Given the established role of geranylgeranylation in membrane protein trafficking, we performed plasma membrane proteomics in FDPS-knockdown B16F10 cells (Fig. 2H). This analysis revealed a pronounced reduction in membrane-associated PD-L1 (Fig. 2I), implicating PD-L1 trafficking as a key downstream target of the MVA pathway. We therefore hypothesized that FDPS loss sensitizes tumor cells to CD8$^+$ T cell attack by reducing PD-L1 surface availability. Consistent with this model, the enhanced killing induced by FDPS knockdown was abolished in PD-L1-deficient cells, indicating that the immunomodulatory effect of FDPS loss is largely PD-L1 dependent (Fig. 2J). To directly visualize PD-L1 localization, we expressed mCherry-tagged PD-L1 in B16F10 cells and found that FDPS knockdown markedly reduced its membrane localization (Fig. 2K). Decreased surface PD-L1 was further confirmed by flow cytometry and by immunoblotting of isolated plasma membrane fractions from FDPS-depleted tumor cells (Fig. 2L-O). Although FDPS inhibition modestly reduced PD-L1 mRNA and total protein abundance (Fig. 2L, M and P), surface PD-L1 remained decreased after blocking transcription with actinomycin D (ActD) or translation with cycloheximide (CHX) (Fig. 2Q), supporting a direct effect on PD-L1 trafficking. Together, these data indicate that the MVA pathway regulates PD-L1 predominantly by modulating its post-translational trafficking to the plasma membrane.

Next, we performed rescue experiments in FDPS-inhibited cells by supplementing FPP, GGPP, or cholesterol. Immunofluorescence and flow cytometry showed that GGPP fully restored PD-L1 membrane localization, whereas FPP produced a partial rescue and cholesterol supplementation had no effect (Supplementary Fig. 2H, I). Neither genetic silencing of farnesyltransferase (Fntb-KD) nor pharmacologic inhibition with tipifarnib reduced PD-L1 membrane levels (Supplementary Fig. 2J, K). By contrast, genetic knockdown of geranylgeranyltransferase (Pggt1b-KD) or pharmacologic inhibition with GGTi-298 markedly decreased PD-L1 surface expression (Supplementary Fig. 2L, M). Finally, inhibition of GGPPS, which blocks GGPP production, likewise reduced PD-L1 membrane levels (Supplementary Fig. 2N-P), further supporting geranylgeranylation as the key modification controlling PD-L1 surface presentation.

RalB regulates PD-L1 surface localization through its geranylgeranylation-dependent activity

Because PD-L1 lacks a C-terminal CAAX motif and therefore cannot be prenylated [9], we hypothesized that FDPS regulates PD-L1 membrane trafficking indirectly through prenylation of PD-L1-associated trafficking proteins. To identify candidate mediators, we intersected the PD-L1 interactome with curated prenylated proteins, highlighting RalB, Rab1a, and Rhog (Fig. 3A). Co-immunoprecipitation confirmed an interaction between PD-L1 and RalB, as well as the RalB effector Ralbp1 (Fig. 3B). To test whether FDPS activity modulates RalB prenylation, we used an established alkynyl-isoprenol reporter (alk-FOH), a surrogate substrate for FTase and GGTase-I [10]. In RalB-overexpressing cells with FDPS knockdown or overexpression, alk-FOH labeling followed by click conjugation to azido-rhodamine and in-gel fluorescence analysis showed that FDPS overexpression reduced reporter incorporation into RalB (Fig. 3C), consistent with altered availability of endogenous FPP/GGPP. In parallel, membrane fractionation revealed a redistribution of RalB from the membrane to the cytosol in FDPS-knockdown cells (Supplementary Fig. 3A, B), further supporting impaired RalB geranylgeranylation.

We next assessed whether RalB and the effector Ralbp1 regulate PD-L1 membrane abundance and found that either genetic knockdown of RalB and Ralbp1 using shRNAs or pharmacological inhibition of RalB with BQU57 markedly reduced PD-L1 surface expression (Fig. 3D–H; Supplementary Fig. 3C-I). The ability of FDPS to regulate PD-L1 membrane levels was lost in cells depleted of RalB or Ralbp1 (Supplementary Fig. 3J-M), indicating that FDPS controls PD-L1 in a RalB/Ralbp1-dependent manner. Total PD-L1 protein was also reduced after RalB or Ralbp1 knockdown (Fig. 3G, H; Supplementary Fig. 3G, H), raising the possibility of transcriptional contribution. However, transcriptional and translational blockade experiments showed that the RalB/Ralbp1 axis continued to regulate PD-L1 surface levels even when PD-L1 transcription or translation was inhibited (Fig. 3I; Supplementary Fig. 3N), supporting a post-translational trafficking mechanism. To test whether RalB activity is required, we rescued RalB-depleted cells by re-expressing different activity mutants. Flow cytometry and immunofluorescence confirmed that wild-type (WT) and constitutively active RalB (G23V) restored surface PD-L1, whereas inactive (G26A) or prenylation-deficient (C203S) mutants failed to do so (Fig. 3J, K). Together, these results establish that RalB regulates PD-L1 membrane localization through geranylgeranylation-dependent activity.

To determine how RalB sustains PD-L1 surface levels, we tracked pre-labeled PD-L1 following internalization and recycling (Fig. 3L) [11]. Loss of RalB or Ralbp1 markedly reduced the amount of PD-L1 returned to the cell surface (Fig. 3M). In control cells, primaquine, an inhibitor of endocytic recycling, triggered rapid depletion of surface PD-L1, indicating that a substantial fraction of surface PD-L1 undergoes continuous internalization and recycling. In contrast, primaquine caused little additional loss of surface PD-L1 in RalB- or Ralbp1-depleted cells (Fig. 3M), consistent with a pre-existing defect in endocytic recycling. To directly quantify recycling kinetics, we used an established recycling assay [11] in which internalized, fluorescently labeled PD-L1 was tracked after quenching surface fluorescence. Recycling was calculated from the reappearance of quenchable surface signal. Control cells recycled most internalized PD-L1 within 10-15 minutes, whereas recycling was significantly impaired in cells lacking RalB or Ralbp1 (Fig. 3N, O).

RalB regulates PD-L1 transcription through NF-κB and STAT3

The reduction in total PD-L1 protein upon RalB or Ralbp1 knockdown prompted us to test whether PD-L1 is also regulated at the transcriptional level. PD-L1 mRNA was reduced after knockdown of RalB or Ralbp1 (Fig. 3G, H; Supplementary Fig. 3G, H; Supplementary Fig. 4A, B). Rescue experiments further confirmed that RalB regulates PD-L1 transcription in an activity-dependent manner (Supplementary Fig. 4C). To define the underlying mechanism, we performed RNA-seq in control and

RalB-knockdown B16F10 cells. GSEA revealed suppression of PD-L1-related gene signatures upon RalB loss, together with marked downregulation of NF-κB signaling (Supplementary Fig. 4D). Consistently, phosphorylation of NF-κB was reduced in RalB-deficient cells (Supplementary Fig. 4E). In parallel, screening additional reported PD-L1 transcriptional regulators showed reduced STAT3 phosphorylation upon RalB depletion (Supplementary Fig. 4E). Functionally, genetic or pharmacologic inhibition of STAT3 or NF-κB individually decreased PD-L1 mRNA (Supplementary Fig. 4F–I), and combined disruption of STAT3 and NF-κB abolished RalB-dependent regulation of PD-L1 transcription (Supplementary Fig. 4J). Together, these data indicate that RalB promotes PD-L1 transcription through STAT3 and NF-κB.

Inhibition of the RalB/Ralbp1 axis sensitizes tumor cells to CD8$^+$ T cell-mediated cytotoxicity

We next assessed the functional contribution of RalB and Ralbp1 to tumor growth and CD8$^+$ T cell activity in vitro and in vivo. Knockdown of RalB or Ralbp1 enhanced antigen-specific CD8$^+$ T cell cytotoxicity in coculture assays (Fig. 4A-D) and suppressed tumor growth in immunocompetent mice (Fig. 4E, F). Immune profiling further showed that depletion of either RalB or Ralbp1 increased intratumoral CD8$^+$ T cell infiltration and was accompanied by an enrichment of GZMB$^+$ CD8$^+$ T cells (Fig. 4G, H). Together, these data establish the RalB/Ralbp1 complex as a key tumor-intrinsic regulator that limits CD8$^+$ T cell-mediated antitumor immunity.

Pharmacological inhibition of FDPS sensitizes tumor cells to immune checkpoint blockade

Our mechanistic data identify FDPS as a tumor-intrinsic driver of immune evasion by sustaining PD-L1 transcription and surface availability through the GGPP-RalB axis, thereby limiting CD8$^+$ T cell effector function. Because FDPS is directly druggable by nitrogen-containing bisphosphonates (N-BPs) that are already used clinically, we hypothesized that pharmacologic FDPS inhibition would dismantle PD-L1-mediated immune suppression and enhance the efficacy of immune checkpoint blockade. To stringently test this hypothesis, we used the B16F10 subcutaneous melanoma model, which is resistant to anti-PD-1 monotherapy, and evaluated risedronate in combination with anti-PD-1. The combination produced markedly improved tumor control compared with either treatment alone (Fig. 5A-C). To assess whether this benefit generalizes across checkpoint backbones and across N-BPs with different potency, we combined zoledronate, the most potent clinically used N-BP, with anti-CTLA-4 in B16F10 melanoma. While zoledronate and anti-CTLA-4 each impeded tumor growth as monotherapies, the combination achieved substantially greater antitumor activity (Fig. 5D-F). At the doses tested, neither zoledronate nor risedronate caused detectable toxicity, as assessed by histologic evaluation of major organs and body weight during monotherapy or combination treatment (Fig. 5G-I).

To investigate how combination therapy alters tumor-infiltrating immune cells, we profiled leukocytes from B16F10 tumors treated with zoledronate and anti-CTLA-4. Compared with control and monotherapy, the combination significantly increased the proportion of intratumoral CD8$^+$ T cells (Fig. 5J). We further analyzed lymphocyte and myeloid populations in tumor-draining lymph nodes and spleen and did not detect significant changes across groups (Supplementary Fig. 5A-D). Collectively, these findings support the immunotherapeutic potential of FDPS-targeting N-BPs and suggest that they enhance checkpoint efficacy by strengthening intratumoral CD8^{+} T cell cytotoxicity.

Human T cells and clinical correlation analyses

To establish translational relevance of the FDPS-RalB axis, we first confirmed that inhibition of FDPS or RalB reduced PD-L1 surface levels in human melanoma and colorectal cancer cell lines, including A375, SK-MEL-103, RKO, and HCT116 (Fig. 6A-H). We next evaluated functional consequences in human T cells using an antigen-specific coculture model. Naïve CD8^{+} T cells from healthy donor PBMCs were engineered to express an NY-ESO-1-specific TCR (ESO-TCR) and cocultured with A375 melanoma cells engineered to express NY-ESO-1 and HLA-A2 (A375-A2-ESO) (Fig. 6I) [12, 13]. Under these conditions, knockdown of FDPS or RalB in tumor cells significantly increased killing by activated ESO-TCR^{+} CD8^{+} T cells (Fig. 6J). To examine clinical associations, we analyzed TCGA melanoma and colorectal cancer datasets using TIMER 2.0. FDPS expression negatively correlated with estimated CD8^{+} T cell infiltration in both tumor types, whereas RalB expression positively correlated with PD-L1 expression (Fig. 6K-L). In melanoma, higher FDPS expression was also associated with poorer overall survival (Fig. 6M). Together, these data support conservation of the FDPS-RalB pathway in human cancers and link elevated FDPS to reduced T cell infiltration and adverse outcomes, providing a rationale for repurposing nitrogen-containing bisphosphonates as combination partners for immunotherapy.

Discussion

This study identifies a tumor-intrinsic mechanism linking the mevalonate pathway to immune evasion. FDPS shapes downstream isoprenoid metabolites, alters GGPP availability, and thereby regulates geranylgeranylation-dependent activity of RalB. This axis supports PD-L1 transcription and maintains PD-L1 surface availability through endocytic recycling. Disrupting FDPS or the downstream geranylgeranylation machinery increases CD8^{+} T cell infiltration and effector function, enhances antigen-specific T cell cytotoxicity in coculture, and suppresses tumor growth in immunocompetent settings. Together, these data support an FDPS-GGPP-RalB pathway as a tumor-cell program that couples lipid metabolism to checkpoint control.

The MVA pathway is essential for cholesterol biosynthesis and protein prenylation, and prior work has emphasized direct effects on immune cells. Dysregulated mevalonate intermediates can activate Vγ9Vδ2 T cells through BTN3A1-dependent sensing [14-16]. Cholesterol accumulation in the tumor microenvironment can promote CD8^{+} T cell dysfunction and increase inhibitory receptor expression [8], whereas membrane cholesterol in CD8^{+} T cells can also enhance TCR clustering and signaling to support early activation and immune synapse formation [17]. Beyond T cells, FPP-dependent RhoA prenylation was shown to preserve the survival and functions of migratory dendritic cells [18]. In contrast, mechanisms by which tumor-intrinsic mevalonate flux remodels the tumor microenvironment remain less defined. Our data point to GGPP-dependent geranylgeranylation as an important branch limiting tumor susceptibility to $CD8^+$ T cell attack. These results provide a framework for considering how distinct mevalonate outputs can have non-overlapping immunological consequences.

PD-L1 is regulated by inducible transcriptional programs and by post-translational processes that control its surface levels [19]. Cytokine-driven pathways and oncogenic programs can induce PD-L1 transcription through factors such as IRF1, NF-κB, and STAT3, with additional context-specific regulators described across tumor types [20-24]. Independently, PD-L1 is processed and trafficked to the plasma membrane, where it undergoes constitutive internalization and recycling [11, 25, 26]. Multiple factors have been reported to stabilize PD-L1 at the surface or divert it toward lysosomal degradation, including CMTM family proteins and recycling endosome-associated adaptors such as TRAPPC4 and RAB11, as well as factors that promote endolysosomal routing [11, 27-29]. Our work adds mevalonate metabolism to PD-L1 regulation by identifying the FDPS-GGPP-RalB axis as an upstream driver of both PD-L1 recycling and transcription. At the trafficking level, RalB and Ralbp1 are required to sustain PD-L1 recycling and surface localization, providing a mechanistic explanation for the loss of membrane PD-L1 after FDPS inhibition. At the transcriptional level, RalB supports PD-L1 mRNA abundance through NF-κB and STAT3 activity. The mechanism connecting RalB to NF-κB and STAT3 activation remains to be clarified.

Targeting the MVA pathway has attracted interest as an immunotherapy-adjunct strategy, yet the tumor-intrinsic mechanisms linking MVA metabolism to immune escape have remained insufficiently defined. Statins inhibit HMG-CoA reductase and were initially suggested to have tumor-suppressive activity based on clinical observations beyond their cardiovascular indications [5-7]. Subsequent studies have associated statin use with improved survival across multiple cancers [30, 31] and with enhanced efficacy of immune checkpoint blockade in several settings, including breast cancer [32, 33], multiple myeloma [34], ovarian cancer [35], non-small cell lung cancer [36], and hepatocellular carcinoma [37]. Atorvastatin has also been reported to reduce expression of inhibitory receptors including PD-1, CTLA-4, TIM-3, and LAG-3 in T cells [38], further implicating MVA pathway activity in checkpoint programs. Our findings provide a tumor-intrinsic mechanistic basis for these clinical associations by defining an FDPS-GGPP-RalB axis that reinforces PD-L1 immune evasion through dual control of PD-L1 transcription and surface recycling, thereby supporting evaluation of FDPS-targeting nitrogen-containing bisphosphonates as rational sensitizers for immune checkpoint blockade.

Nitrogen-containing bisphosphonates (N-BPs) have limited oral bioavailability and, after absorption, a substantial fraction is rapidly sequestered in bone [39]. This pharmacokinetic profile complicates targeting extra-skeletal tumors because drug exposure in soft tissues can be variable and potentially limited by bone uptake. Approaches that mitigate this constraint, including parenteral dosing to reduce absorption variability and formulation strategies that improve tissue distribution such as lipophilic adjuvant platforms, may therefore be important when considering N-BPs for systemic immunooncology applications. In support of this concept, lipophilic statins and bisphosphonates have been reported to function as potent vaccine adjuvants [40], consistent with broader immunomodulatory consequences of perturbing mevalonate metabolism. At the same time, the bone tropism of N-BPs is advantageous in skeletal disease. N-BPs are widely used in patients with bone metastases, particularly in breast cancer, where extensive clinical experience supports benefit [41-43]. Mechanistically, bisphosphonates suppress bone resorption by inducing osteoclast apoptosis, which is accompanied by reduced metastatic burden in bone in experimental models [44-46]. Our findings suggest that, beyond osteoclast-targeted effects, FDPS inhibition can provide an additional therapeutic layer by enhancing antitumor immunity and improving responses to checkpoint blockade. This supports evaluation of N-BPs as immunotherapy combination partners in bone metastatic disease, while emphasizing that rational dosing and delivery will likely be required to extend benefit to extra-skeletal tumors.

In summary, our data support a model in which isoprenoid metabolites downstream of the mevalonate pathway restrain CD8$^+$ T cell antitumor immunity by sustaining PD-L1 surface expression on tumor cells, thereby promoting immune evasion. We further show that pharmacologic inhibition of this pathway at FDPS, using clinically established nitrogen-containing bisphosphonates, enhances the efficacy of PD-1 blockade in vivo. These findings provide a mechanistic rationale to evaluate N-BPs as immunotherapy combination partners and to investigate biomarkers of pathway engagement and response in patients. More broadly, they highlight tumor-intrinsic mevalonate metabolism as a tractable metabolic axis that can shape checkpoint control and merits deeper study as part of the regulatory network governing antitumor immunity.

Methods

Tumor cell lines

Mouse melanoma cell line B16F10, mouse colorectal cancer cell line MC38, human melanoma cell line A375 and SK-MEL-28, human colorectal cancer cell lines RKO and HCT116 were obtained from American Type Culture Collection (ATCC). B16F10 and MC38 cells were cultured in RPMI 1640 medium (Gibco; cat. #C11875500BT). All other cells were cultured in Dulbecco’s modified Eagle’s medium (DMEM) (Gibco; cat. #C11995500BT). All cultured medium were supplemented with 10% FBS (Gibco; cat. #A5669701), 100 units/mL penicillin and 100 µg/mL streptomycin (Gibco; cat. #15140122).

CD8$^+$ T cells isolation and activation

Primary naïve CD8$^+$ T cells were purified from spleens and inguinal lymph nodes of OT-1 mice using a naïve CD8a$^+$ T cell isolation kit (Miltenyi Biotec; cat. #130-117-044). The cells were activated for 72 hours at 37°C in plates coated with 2.5 µg/mL anti-CD3e (clone 145-2C11; Invitrogen ; cat. 16-0031-82) and 2.5 µg/mL anti-CD28 (clone 37.51; Invitrogen; cat. #16-0281-82) in the RPMI 1640 medium

(Gibco #C11875500BT) presence of 100 units/mL IL2 (PEPROTECH; cat. #212-12) and 50 µmol/L β-mercaptoethanol (Sigma-Aldrich; cat. #M620).

In vitro killing assay

For killing assays, 20,000 OVA-GFP-expressing target tumor cells were seeded per well in flat-bottom 96-well plates. After 12 hours, OT-1 CD8$^+$ T lymphocytes were added to designated wells at effector-to-target (E:T) ratios of 1:6 for B16F10 cells or 1:3 for MC38 cells. Cocultures were maintained in RPMI-1640 medium supplemented with 10% FBS (Gibco; cat. #A5669701), 100 U/mL penicillin, and 100 µg/mL streptomycin (Gibco, cat. #15140122). Following 24 hours of coculture, GFP-positive tumor cells were imaged using a fluorescence microscope, and the percentage of tumor cell confluence was quantified using ImageJ software.

Human CD8$^+$ T cell activation and transductions

Healthy donor PBMCs were purchased from Milecell Biotechnology Co., Ltd. (Shanghai, China) without donor identifiers, in accordance with applicable federal and state regulations. PBMCs were thawed and rested at 1 × 10^6 cells/ml in RPMI-1640. CD8α$^+$ T cells were isolated using a CD8α$^+$ T cell isolation kit (Xinbio; cat. #51-01-0002) and stimulated with plate-bound anti-human CD3 (2.5 µg/ml; Invitrogen; cat. #16-0037-81) and soluble anti-human CD28 (2.5 µg/ml; Invitrogen; cat. #16-0289-81) in RPMI-1640 supplemented with 10% FBS, 25 mM HEPES (Gibco; cat. #15630080), 1 mM sodium pyruvate (Gibco; cat. #11360070), 1× Pen/Strep (Gibco; cat. #15140122), 1× NEAA (Gibco; cat. #11140050), human IL-2 (10 ng/ml; NOVOPROTEIN; cat. #C013), and 50 µM β-mercaptoethanol (Sigma-Aldrich; cat. #M620). After 48 h of activation, CD8$^+$ T cells were transduced with an NY-ESO-1–specific TCR to generate NY-ESO-1 TCR-T cells. The NY-ESO-TCR-mCherry plasmid was obtained from Addgene and subcloned into a lentiviral backbone by recombination. Lentivirus was produced in 293T cells. For transduction, activated CD8$^+$ T cells were spin-infected with viral supernatant supplemented with polybrene (10 µg/ml; Merck; cat. #TR-1003-G) at 660g and 30°C for 90 min in retronectin-coated, non–tissue culture-treated 6-well plates. Cells were then incubated at 37°C and the medium was replaced with fresh complete medium after 3 h. Transduced CD8$^+$ T cells were expanded for an additional 7–10 days and cryopreserved for subsequent coculture assays.

Lentivirus-delivered shRNA knockdown and gene overexpression in cancer cells

All shRNA and overexpression constructs were obtained from IGE Biotechnology Co., Ltd. (Guangzhou, China). The designed shRNA sequences were cloned into the pLKO.1-puro lentiviral vector. Recombinant lentiviral particles were generated by co-transfecting 293T cells with the plasmid transfer along with the packaging plasmids psPAX3 (3.25 µg) and the envelope plasmid pMD2.G (1.75 µg) using polyethylenimine linear (PEI; Polysciences, cat. #23966-100) according to standard protocols. Viral supernatants were harvested 48 h post-transfection and filtered through a 0.45 µm membrane. Target cells were infected in the presence of 8 µg/ml polybrene (Merck, cat. #TR-1003-G) for 24 h, followed by selection with 2 µg/ml puromycin (TargetMol, cat. #T2219) to establish stable populations.

Animals

Six- to ten-week-old mice were used for all experiments. Wild-type C57BL/6J mice and nude mice were purchased from the GemPharmatech Co., Ltd. (Suzhou, China,). OT-1 (C57BL/6JCya-Tg (Tcra-V2, Tcrb-V5)/Cya) mice were purchased from Cyagen Biosciences (Suzhou, China) and bred in-house. Mice were bred and maintained in individually ventilated cages and fed with autoclaved food and sterile water at Animal Facility of Shenzhen Bay Laboratory. All animal experiments were performed in accordance with protocols approved by the Animal Research Ethics Committee of Shenzhen Bay Laboratory (Approved Protocol ID: AEYCQ202103) according to national and institutional guidelines.

Subcutaneous tumor model

Six- to eight-week-old female C57BL/6J mice and nude mice were inoculated subcutaneously in the right flank with 3×10^5 and 5×10^4 B16F10 cells, respectively. Tumors were monitored for 15 days, with body weight and tumor volume measured at regular intervals throughout the study. Tumor volume was calculated using the formula: $(\text{length} \times \text{width}^2) / 2$, where length and width represent the longest and perpendicular shortest diameters in millimeters, respectively. At the endpoint, solid tumors were excised, and tumor-infiltrating immune cells (TIIs) were isolated for subsequent flow cytometric analysis.

Flow cytometry

Cancer cells or isolated tumor-infiltrating immune cells were collected and washed with protein-free PBS. The cells were then stained with Zombie UV™ Fixable Viability Dye (BioLegend; cat. #423107), diluted 1:500 in PBS, for 30 minutes at room temperature in the dark. After washing with FACS buffer (PBS containing 2% FBS), Fc receptors were blocked prior to surface staining using either mouse TruStain FcX™ plus (BioLegend; cat. #156604; 1:200 dilution) or human TruStain FcX™ (BioLegend; cat. #422302; 1:100 dilution) for 10 minutes at 4 °C. Subsequently, surface proteins were stained with corresponding fluorophore-conjugated antibodies for 30 minutes at 4 °C. If intracellular protein staining was required, following surface staining, cells were fixed and permeabilized using commercially available fixation/permeabilization reagents (Thermo Fisher Scientific; cat. # 00-5523-00) according to the manufacturer’s protocol, followed by staining for intracellular targets at room temperature for 30 minutes. Staining was terminated by washing with FACS buffer. Data were acquired on a CytoFLEX LX flow cytometer (Beckman Coulter) and analyzed using CytExpert (Beckman Coulter) or FlowJo software.

Real-time quantitative PCR (qPCR) assays

Total RNA was extracted using the Super FastPure Cell RNA Isolation Kit (Vazyme; cat. # RC102-01) according to the manufacturer’s instructions. First-strand cDNA synthesis was performed with the RevertAid First Strand cDNA Synthesis Kit (Thermo Fisher Scientific; cat. # K16225) following the supplier's protocol. Quantitative real-time PCR (qPCR) was conducted in triplicate using 2× SYBR Green qPCR Master Mix (Selleck; cat. # B21202) on a CFX96 Touch™ Real-Time PCR Detection System (Bio-Rad). GAPDH was used as the internal reference gene. Relative expression levels were calculated using the ΔΔCT method.

Western blotting

Cells were washed three times with ice-cold PBS and lysed on ice for 30 min using RIPA lysis buffer (Beyotime; cat. #P0013C) supplemented with protease (Selleck; cat. #B14001) and phosphatase (Selleck; cat. #B15001) inhibitor cocktails. Lysates were sonicated briefly and cleared by centrifugation at 12,000 × g for 15 min at 4 °C. Protein concentration was determined with a BCA Protein Assay Kit (Thermo Fisher Scientific; cat. #23227). Equal amounts of protein from each sample were separated by SDS-PAGE and transferred onto polyvinylidene difluoride (PVDF) membranes (Merck; cat. #IPVH00010) using a wet-transfer system at 100 V for 2 h. Membranes were blocked with 5% non-fat milk (Sangon Biotech; cat. #A600669-0250) in Tris-buffered saline containing 0.1% Tween-20 (TBST) for 1 h at room temperature, followed by incubation with primary antibodies overnight at 4 °C. After washing, membranes were incubated with appropriate HRP-conjugated secondary antibodies. Protein bands were visualized using Clarity Western ECL Substrate (Bio-Rad; cat. #1705061) and imaged with a chemiluminescence detection system.

Co-immunoprecipitation (Co-IP)

For co-immunoprecipitation assays, cells were washed three times with ice-cold PBS and lysed on ice for 30 min in NP-40 lysis buffer supplemented with protease and phosphatase inhibitors. Lysates were centrifuged at 15,000 × g for 15 min at 4 °C. A total of 250 μg of supernatant protein was incubated with either anti-Flag magnetic beads (MedChemExpress; cat. #HY-K0202) or anti-HA magnetic beads (Thermo Fisher Scientific; cat. #88836) for 1 h at room temperature. Beads were collected using a magnetic stand and washed three times with lysis buffer. Bound proteins were eluted, separated by SDS-PAGE, and analyzed by immunoblotting with the indicated antibodies.

Immunofluorescence staining

Cells grown on sterile coverslips in 6-well plates were washed once with 1× PBS and fixed with 4% paraformaldehyde (PFA) for 20 min. After permeabilization with 0.2% Triton X-100 for 20 min, cells were blocked with 3% bovine serum albumin (BSA) for 1 h at room temperature. Samples were then incubated with primary antibody overnight at 4 °C, followed by incubation with appropriate secondary antibody for 1 h at room temperature. Nuclei were counterstained with Hoechst 33342 (Invitrogen; cat. #H3570; diluted 1:10,000). Finally, coverslips were mounted onto glass slides using Mowiol® 4-88 mounting medium (Sigma-Aldrich; cat. #81381). Fluorescence images were acquired with a confocal laser-scanning microscope (Carl Zeiss LSM980) using appropriate laser lines and filter settings.

Protein profiling by mass spectrometry

For plasma membrane profiling, cells were harvested and lysed with a Plasma Membrane Protein Isolation Kit (Invent, cat # SM-005); Protein concentration was determined using the BCA Protein Assay Kit (Thermo Fisher Scientific, cat. #23227). For PD-L1 protein interactionomics, cells were collected and lysed in NP-40 lysis buffer (Beyotime; cat. #P0013F) containing a protease inhibitor cocktail (Selleck; cat. #B14001). Lysates were centrifuged at 16,000 × g for 20 min at 4 °C, and the supernatant was collected. Protein concentration was measured using the BCA Protein Assay Kit (Thermo Fisher Scientific, cat. #23227). Target proteins were immunoprecipitated with anti-Flag magnetic beads. After washing with NP-40 buffer, beads were resuspended in Elution Buffer (Thermo Scientific, cat. #21028) and incubated at 37 °C with shaking (1000 rpm) for 1 h to elute bound proteins. Then, proteins were reduced with 50 mM dithiothreitol (DTT) at 60 °C for 45 min, followed by alkylation with 100 mM iodoacetamide (IAA; Merck, cat. #I1149) for 1 h in the dark. Samples were then diluted 1:4 with 50 mM Tris-HCl (pH 8.0) to reduce the urea concentration to 2 M. Digestion was performed overnight (12–16 h) at 37 °C with trypsin at a 1:50 enzyme-to-substrate ratio under constant shaking. The resulting peptides were acidified with 1% formic acid (final concentration) and centrifuged at 2,000 g for 5 min to remove precipitated urea. Peptide desalting was carried out using Pierce™ C18 Spin Columns (Thermo Scientific, cat. #60108-302). Columns were activated with 200 µL of 50% acetonitrile (ACN; Merck, cat. #34851) and centrifuged at 1,500 × g for 1 min; this step was repeated once. Columns were equilibrated twice with 200 µL of 0.5% trifluoroacetic acid (TFA; Merck, cat. #302031) in 5% ACN. Peptide samples were diluted with 2% TFA in 20% ACN (1 µL per 3 µL sample), loaded onto the resin bed, and centrifuged at 1,500 × g for 1 min; the flow-through was reloaded twice to maximize binding. Columns were washed three times with 200 µL of 0.5% TFA in 5% ACN. Peptides were eluted with 20 µL of 70% ACN (repeated three times) into a fresh tube and dried. The dried peptides were reconstituted in 20 µL of 0.1% formic acid, and peptide concentration was measured at 205 nm using a Nanodrop spectrophotometer. Samples were adjusted to 250 ng/µL, centrifuged at 14,000 × g for 5 min, and the supernatant was transferred to MS vials. Samples were analyzed on an Easy nLC 1200 system (Thermo Fisher Scientific) coupled online to an Orbitrap Fusion Lumos mass spectrometer equipped with a nanospray flex ion source (Thermo Fisher Scientific). Raw MS files were processed using Proteome Discoverer software (v2.5, Thermo Fisher Scientific) for protein identification and quantification.

Click Chemistry Assay

The AlK-FOH probe was synthesized following the protocol reported by Charron et al. [10]. Cells were treated with 50 µM Alk-FOH for 6 hours, harvested, and lysed in lysis buffer (100 mM Tris-HCl pH 7.2, 5 mM EDTA, 150 mM NaCl, 2.5% SDS) supplemented with a protease inhibitor cocktail. After centrifugation at 16,000 × g for 20 min at 4 °C, the supernatant was collected. Protein concentration was determined using a BCA Protein Assay Kit (Thermo Fisher Scientific; cat. #23227). Target proteins were isolated using anti-HA magnetic beads (Thermo Fisher Scientific; cat. #88836). The beads were washed and resuspended in 50 µl of immunoprecipitation wash buffer. Click chemistry reagents were then added in the following order: 1 µl of 4 mM TAMRA azide (Lumiprobe; cat. #47130), 1.2 µl of 10 mM tris[(1-benzyl-1H-1,2,3-triazol-4-yl)methyl]amine (TBTA; Sigma-Aldrich; cat. #678937), 1 µl of 40 mM $CuSO_4$ (Sigma-Aldrich; cat. #451657), and 1 µl of 40 mM tris(2-carboxyethyl)phosphine hydrochloride (TCEP-HCl; Sigma-Aldrich; cat. #C4706). The reaction mixture was vortexed thoroughly and incubated for 30 min in the dark at room temperature. Subsequently, 20 µl of 4× SDS loading buffer was added, and samples were heated at 95 °C for 10 min. Proteins were separated by SDS-PAGE. The gel was briefly rinsed with water and then scanned using a ChemiDoc MP Imaging system (Bio-Rad) to detect rhodamine fluorescence. Afterwards, the gel was destained with shaking for 2–8 h in destaining buffer (50% methanol, 40% water, 10% acetic acid), followed by incubation in water to reduce background. After a final scan, the gel was stained with Coomassie Brilliant Blue (Sigma; cat. #B7920) to verify equal protein loading.

Internalization assay

Cells were detached with trypsin and kept on ice. After a single wash with RPMI 1640 medium containing 5% FBS and 30 mM HEPES (used for all subsequent staining and wash steps), surface PD-L1 was labeled by incubating cells with an unconjugated anti-PD-L1 primary antibody (BioLegend; cat. #124302) for 30 min on ice. Unbound antibody was removed by two washes. Cells were then resuspended in complete RPMI 1640 medium on ice, and a baseline sample was taken and maintained on ice. The remaining cells were transferred to a 37°C incubator to allow antibody-labeled PD-L1 internalization, either in the presence or absence of 300 µM primaquine (TargetMol; cat. # T60411). Samples were collected at 15, 30, and 45 min, and immediately diluted in ice-cold phosphate-buffered saline (PBS) to halt further endocytosis. Following two washes, residual surface-bound primary antibody was detected by staining with an APC-conjugated anti-mouse secondary antibody (BioLegend; cat. #405308) for 30 min on ice. After two final washes, samples were analyzed by flow cytometry.

Recycling assay

Cells were labelled with a PE-conjugated PD-L1-specific antibody (BioLegend; cat. # 124308) at 4 °C for 30min, washed out the unbound antibody and incubated at 37 °C for 30min to allow internalization. Residual cell surface-bound antibody was then quenched by treatment with a low-pH buffer (0.5 M NaCl, 0.5% acetic acid, pH 2.5–2.8) for 2 min on ice, followed by neutralization with RPMI 1640 containing 5% FBS and 30 mM HEPES. A baseline sample was maintained on ice throughout the procedure. The remaining samples were returned to 37°C and incubated for 5, 10, or 15 min to permit recycling of the internalized PD-L1. Recycled antibody-labeled PD-L1 on the cell surface was subsequently re-quenched using the same low-pH treatment. Remaining intracellular antibody-labeled PD-L1 was detected by flow cytometry. After normalizing for incomplete quenching by subtracting the quenchable fluorescence signal in the baseline (time zero) sample, the fluorescence intensity of recycled PD-L1 at each time point was compared to the total internalized PD-L1 signal obtained after the initial endocytosis step to calculate the percentage of PD-L1 recycled.

Statistical analysis

Statistical analyses were performed using GraphPad Prism software (version 10.4.0). Data are presented as mean ± standard deviation (SD). Each experiment was independently replicated at least three times or involved more than six mice per group where applicable. Differences between groups were assessed using Student's t-test, one-way analysis of variance (ANOVA), or two-way ANOVA, as appropriate. Correlations were evaluated using Pearson's correlation coefficient.

Acknowledgements

This work was supported by Shenzhen Medical Research Fund (B2302018 and B2502037), National Key R&D Program of China (2022YFA0912600), National Natural Science Foundation of China (82341011 and 82572993), and Major Program (S201101004) of Shenzhen Bay Laboratory. The authors are grateful to Biochemical Analysis Core, Multi-omics Mass Spectrometry Core, Bio-Imaging Core, and Animal Laboratory Center of Shenzhen Bay Laboratory for help with technical assistance.

Author Contributions

M.H. and C.Y. provided conceptualization and wrote the original draft. M.H., J.Z., Y.H., B.H., W.K., D.L., Y.W., Y.Z., H.W., Y.Z., Y.H., Y.W., and Y.N. performed the experiments and analyzed the data. C.Y. and L.Z. reviewed and edited the paper. C.Y. provided supervision and resources and performed funding acquisition.

Competing interests

The authors declare no competing interests.

Data, code, and materials availability

All data are available in the main text or the supplementary materials. To request the materials related to the study, please contact the corresponding author.

Figure legends

Figure 1. Inhibition of the MVA pathway sensitizes tumor cells to CD8+ T cell cytotoxicity

A. Schematic of the mevalonate pathway highlighting HMGCR and FDPS with downstream branches for cholesterol biosynthesis and isoprenoid-dependent protein prenylation.
B. Tumor growth curves of B16F10-shCtrl and B16F10-shFDPS allografts in immunocompetent C57BL/6 mice.
C. Tumor weights of B16F10-shCtrl and B16F10-shFDPS allografts in C57BL/6 mice at the experimental endpoint.
D. Tumor growth curves of B16F10-shCtrl and B16F10-shFDPS tumors in nude mice.
E. Tumor weights of B16F10-shCtrl and B16F10-shFDPS tumors in nude mice at the experimental

endpoint.

F. Percentage of intratumoral $CD8^+$ T cells among $CD45^+$ tumor-infiltrating leukocytes.

G. Quantification of $GZMB^+$ cells within the intratumoral $CD8^+$ T cell population.

H. Quantification of $IFN\gamma^+$ cells within the intratumoral $CD8^+$ T cell population.

I. Tumor growth curves of B16F10-shFDPS allografts in C57BL/6 mice with or without $CD8^+$ T cell depletion.

J. Tumor weights of B16F10-shFDPS allografts in C57BL/6 mice with or without $CD8^+$ T cell depletion at the endpoint.

K. Confluence of monocultured B16-OVA and MC38-OVA cells with or without HMGCR or FDPS knockdown at 24 h.

L. Cytotoxicity assay of B16-OVA and MC38-OVA cells cocultured with OT-1 $CD8^+$ T cells with or without HMGCR and FDPS knockdown at 24 h.

M. Monocultured B16-OVA and MC38-OVA cells treated with DMSO or the indicated inhibitors, simvastatin (2.5 μM), rosuvastatin (10 μM), atorvastatin (10 μM), zoledronate (10 μM), or risedronate (10 μM), with confluence quantified at 24 h.

N. Cytotoxicity assay of B16-OVA and MC38-OVA cells co-cultured with OT-I $CD8^+$ T cells in the presence of DMSO or the indicated inhibitors, simvastatin (2.5 μM), rosuvastatin (10 μM), atorvastatin (10 μM), zoledronate (10 μM), or risedronate (10 μM), with confluence quantified at 24 h.

O. Cytotoxicity assay of B16-OVA and MC38-OVA cells co-cultured with OT-I $CD8^+$ T cells after tumor-cell pretreatment with DMSO or the indicated inhibitors, simvastatin (2.5 μM), rosuvastatin (10 μM), atorvastatin (10 μM), zoledronate (10 μM), or risedronate (10 μM), with confluence quantified at 24 h.

P. Cytotoxicity assay of B16-OVA and MC38-OVA cells co-cultured with OT-I $CD8^+$ T cells after $CD8^+$ T cell pretreatment with DMSO or the indicated inhibitors, simvastatin (2.5 μM), rosuvastatin (10 μM), atorvastatin (10 μM), zoledronate (10 μM), or risedronate (10 μM), with confluence quantified at 24 h.

Q. Representative images and quantification of GFP-positive lung metastatic foci in C57BL/6 mice 28 days after tail vein injection of B16F10-shCtrl or B16F10-shFDPS cells. Scale bar, 5 mm.

R. Schematic of the tumor rechallenge experiment in C57BL/6 mice. Following surgical resection of the primary subcutaneous B16F10-shFDPS tumors, mice were rechallenged with the B16F10-shCtrl cells on the contralateral flank 14 days later.

S. Tumor growth curves of B16F10-shCtrl tumors in both primary control and in the rechallenge setting in C57BL/6 mice.

T. Kaplan–Meier survival of mice in the primary control group and in the rechallenge setting. Data are mean ± SD from three independent experiments or at least six mice per group. Statistical significance was assessed by Student’s t-test (E, J, F, G, H and Q), two-way ANOVA (B, D, I, L, N and O), or the log-rank test (T).

Figure S1. Inhibition of the MVA pathway sensitizes tumor cells to CD8+ T cell cytotoxicity

A. FDPS mRNA levels in B16F10 cells measured by qPCR.

B. HMGCR mRNA levels in B16F10 cells measured by qPCR.
C. Tumor growth curves of B16F10-shCtrl and B16F10-shHMGCR allografts in C57BL/6 mice.
D. Tumor weights of B16F10-shCtrl and B16F10-shHMGCR allografts in C57BL/6 mice at the experimental endpoint.
E. Growth curves of B16F10-shCtrl and B16F10-shHMGCR tumors in nude mice.
F. Tumor weights of B16F10-shCtrl and B16F10-shHMGCR tumors in nude mice at the experimental endpoint.
G. Representative immunofluorescence staining images of $CD45^+$ immune cell infiltration in B16F10-shCtrl and B16F10-shHMGCR tumors. Scale bar, 50 μm (left). Quantification of $CD45^+$ cells per 1000 total cells (right).
H. Representative immunofluorescence staining images (left) and quantification of $CD8^+$ T cells in B16F10-shCtrl and B16F10-shHMGCR tumors (right). Sale bar, 50 μm.
I. FACS analysis of the proportion of $CD8^+$ T cells among $CD45^+$ tumor-infiltrating leukocytes following $CD8^+$ T cell depletion after anti-CD8α antibody treatment.
J. FDPS mRNA levels in B16F10-OVA and MC38-OVA cells measured by qPCR.
K. HMGCR mRNA levels in B16F10-OVA and MC38-OVA cells measured by qPCR.
L. Cytotoxicity assay of B16-OVA and MC38-OVA cells (shCtrl or shFDPS) co-cultured with OT-I $CD8^+$ T cells and treated with DMSO or the indicated inhibitors, simvastatin (2.5 μM), rosuvastatin (10 μM), atorvastatin (10 μM), zoledronate (10 μM), or risedronate (10 μM).

Data are mean ± SD from three independent experiments or at least five mice per group. Statistical significance was assessed by Student's t-test (D, F, G and H), one-way ANOVA (A, B, J and K), or two-way ANOVA (C, E and L).

Figure 2. The GGPP-dependent geranylgeranylation regulates PD-L1 surface localization on tumor cells to control $CD8^+$ T cells function

A. Effect of FPP, GGPP or cholesterol supplementation on B16F10-shFDPS or MC38-shFDPS cells in monoculture.
B. Cytotoxicity assay of B16-OVA and MC38-OVA cells (shCtrl or shFDPS) co-cultured with OT-1 $CD8^+$ T cells in the presence of FPP, GGPP, cholesterol (20 μM each), or vehicle at 24 h.
C. Cytotoxicity assay of B16-OVA and MC38-OVA cells (shCtrl or shFDPS) co-cultured with OT-I $CD8^+$ T cells after tumor-cell pretreatment with FPP, GGPP, cholesterol (20 μM each), or vehicle, with confluence quantified at 24 h .
D. Cytotoxicity ssay of B16-OVA and MC38-OVA cells (shCtrl or shFDPS) co-cultured with OT-I $CD8^+$ T cells after $CD8^+$ T cell pretreatment with FPP, GGPP, cholesterol (20 μM each), or vehicle, with confluence quantified at 24 h.
E. Schematic of the FPP-to-GGPP branch and protein prenylation.
F. Cytotoxicity assay of B16-OVA and MC38-OVA cells (shCtrl, shFntb, or shPggt1b) co-cultured with OT-I $CD8^+$ T cells at 24 h.
G. Cytotoxicity assay of B16-OVA and MC38-OVA cells co-cultured with OT-I $CD8^+$ T cells in the

presence of GGTi-298 (5 µM), tipifarnib (5 µM), or DMSO at 24 h.

H. Workflow schematic for plasma membrane proteomics of B16F10-shCtrl and B16F10-shFDPS cells by LC–MS/MS.

I. Log2 fold-change of plasma membrane protein abundance in B16F10-shFDPS relative to B16F10-shCtrl cells.

J. Cytotoxicity assay of PD-L1-knockdown B16F10-OVA and MC38-OVA cells co-cultured with $CD8^+$ T cells following FDPS knockdown.

K. PD-L1–mCherry localization in B16F10-shCtrl and B16F10-shFDPS cells. Scale bar, 10 µm.

L. Immunoblot analysis of FDPS and PD-L1 in total lysates, cytosolic, and membrane fractions from B16F10-shCtrl and B16F10-shFDPS cells.

M. Immunoblot analysis of FDPS and PD-L1 in total lysates, cytosolic, and membrane fractions from MC38-shCtrl and MC38-shFDPS cells.

N. Cell-surface PD-L1 expression in B16F10-shCtrl and B16F10-shFDPS cells analyzed by flow cytometry.

O. Cell-surface PD-L1 expression in MC38-shCtrl and MC38-shFDPS cells analyzed by flow cytometry.

P. PD-L1 mRNA levels in B16F10-shCtrl and B16F10-shFDPS cells analyzed by qPCR.

Q. Cell-surface PD-L1 expression in B16F10-shCtrl and B16F10-shFDPS cells treated with 50 nM Actinomycin D (ActD) or 5 ug/ml Cycloheximide (CHX).

Data are the means ± SD from three independent experiments. Statistical significance was assessed by one-way ANOVA (N, O, P and Q) or two-way ANOVA (A, B, C, D, F, G and J).

Figure S2. The GGPP-dependent geranylgeranylation regulates PD-L1 surface localization

A and B. Relative intracellular FPP (A) and GGPP (B) levels in B16F10-shCtrl and B16F10-shFDPS cells measured by LC–MS..

C. Cholesterol levels in B16F10-shCtrl and B16F10-shFDPS cells measured by Filipin III staining and flow cytometry.

D. Fntb mRNA levels in B16F10-OVA and MC38-OVA cells measured by qPCR.

E. Pggt1b mRNA levels in B16F10-OVA and MC38-OVA cells measured by qPCR.

F. Fdft1 mRNA levels in B16F10-OVA and MC38-OVA cells measured by qPCR.

G. Cytotoxicity assay of B16-OVA cells (shCtrl or shFdft1) co-cultured with OT-I $CD8^+$ T cells, with confluence quantified at 24 h .

H. PD-L1–mCherry localization in B16F10-shCtrl cells, B16F10-shFDPS cells, and B16F10-shFDPS cells supplemented with GGPP, FPP, or cholesterol (20 µM each). Scale bar, 10 µm.

I. Cell-surface PD-L1 in B16F10-shCtrl cells, B16F10-shFDPS cells, and B16F10-shFDPS cells supplemented with GGPP, FPP, or cholesterol (20 µM each), measured by flow cytometry.

J. Cell-surface PD-L1 in B16F10-shCtrl and B16F10-shFntb cells measured by flow cytometry.

K. Cell-surface PD-L1 in B16F10 cells treated with tipifarnib (5 µM) or DMSO measured by flow cytometry.
L. Cell-surface PD-L1 in B16F10-shCtrl and B16F10-shPggt1b cells measured by flow cytometry.
M. Cell-surface PD-L1 in B16F10 cells treated with GGTi-298 (5 µM) or DMSO measured by flow cytometry.
N. Ggpps mRNA levels in B16F10 and MC38 cells measured by qPCR.
O. Cell-surface PD-L1 in B16F10-shCtrl and B16F10-shGgpps cells measured by flow cytometry.
P. Cell-surface PD-L1 in MC38-shCtrl and MC38-shGgpps cells measured by flow cytometry.

Data are mean ± SD from three independent experiments. Statistical significance was assessed by Student's t-test (A, B, K and M), one-way ANOVA (C, F, I, J, L, O and P), or two-way ANOVA (D, E, G and N).

Figure 3. RalB regulates PD-L1 surface localization through its geranylgeranylation-dependent activity

A. Venn diagram showing the overlap between PD-L1 interactome and predicted prenylated proteins.
B. Co-immunoprecipitation showing the interaction between Flag-tagged PD-L1 and HA-tagged Ralb or Ralbp1 in B16F10 cells.
C. Click-chemistry assay showing the effect of FDPS knockdown or overexpression on RalB prenylation in RalB-overexpressing B16F10 cells.
D. Cell-surface PD-L1 in B16F10-shCtrl and B16F10-shRalB cells measured by flow cytometry.
E. Cell-surface PD-L1 in B16F10-shCtrl and B16F10-shRalbp1 cells measured by flow cytometry.
F. Cell-surface PD-L1 in B16F10 cells treated with 40 µM BQU57 measured by flow cytometry.
G. Immunoblot analysis of RalB and PD-L1 in total lysates, cytosolic, and membrane fractions from B16F10-shCtrl and B16F10-shRalB cells.
H. Immunoblot analysis of Ralbp1 and PD-L1 in total lysates, cytosolic, and membrane fractions from B16F10-shCtrl and B16F10-shRalbp1 cells.
I. Cell-surface PD-L1 in B16F10-shCtrl and B16F10-shRalB cells treated with 50 nM Actinomycin D (ActD) or 5 µg/ml Cycloheximide (CHX).
J. Cell-surface PD-L1 in B16F10-shCtrl cells, B16F10-shRalB cells, and B16F10-shRalB cells reconstituted with wild-type RalB or the indicated mutants (G23V, G26A, C203S, or G23V/C203S), measured by flow cytometry.
K. PD-L1–mCherry localization in B16F10-shCtrl cells, B16F10-shRalB cells, and B16F10-shRalB cells reconstituted with wild-type RalB or the indicated mutants (G23V, G26A, C203S, or G23V/C203S). Scale bar, 10 µm.
L. Schematic of PD-L1 internalization assay in B16F10 cells.
M. PD-L1 internalization assay in B16F10-shCtrl, B16F10-shRalB, and B16F10-shRalbp1 cells treated with or without primaquine (300 µM), measured by flow cytometry.

N. Schematic of PD-L1 recycling assay in B16F10 cells.

O. PD-L1 recycling assay in B16F10-shCtrl, B16F10-shRalB, and B16F10-shRalbp1 cells measured by flow cytometry.

Data are mean ± SD from three independent experiments. Statistical significance was assessed by Student’s t-test (F) or one-way ANOVA (D, E, I and J).

Figure S3. RalB regulates PD-L1 membrane localization through geranylgeranylation-dependent activity

A. Immunoblot analysis of FDPS and RalB in cytosolic and membrane fractions from B16F10-shCtrl and B16F10-shFDPS cells.

B. Immunoblot analysis of FDPS and RalB in cytosolic and membrane fractions from MC38-shCtrl and MC38-shFDPS cells.

C. RalB mRNA levels in B16F10 and MC38 cells measured by qPCR.

D. Ralbp1 mRNA levels in B16F10 and MC38 cells measured by qPCR.

E. Cell-surface PD-L1 in MC38-shCtrl and MC38-shRalB cells measured by flow cytometry.

F. Cell-surface PD-L1 in MC38-shCtrl and MC38-shRalbp1 cells measured by flow cytometry.

G. Immunoblot analysis of RalB and PD-L1 in total lysates, cytosolic, and membrane fractions from MC38-shCtrl and MC38-shRalB cells.

H. Immunoblot analysis of Ralbp1 and PD-L1 in total lysates, cytosolic, and membrane fractions from MC38-shCtrl and MC38-shRalbp1 cells.

I. PD-L1–mCherry localization in B16F10-shCtrl, B16F10-shRalB, and B16F10-shRalbp1 cells. Scale bar, 10 µm.

J. RalB and FDPS mRNA levels in B16F10 cells measured by qPCR.

K. Ralbp1 and FDPS mRNA levels in B16F10 cells measured by qPCR.

L. Cell-surface PD-L1 in B16F10-shCtrl, B16F10-shRalB, and B16F10-shRalB/shFDPS cells measured by flow cytometry.

M. Cell-surface PD-L1 in B16F10-shCtrl, B16F10-shRalbp1, and B16F10-shRalbp1/shFDPS cells measured by flow cytometry.

N. Cell-surface PD-L1 in B16F10-shCtrl and B16F10-shRalbp1 cells treated with 50 nM Actinomycin D (ActD) or 5 µg/ml Cycloheximide (CHX).

Data are mean ± SD from three independent experiments. Statistical significance was assessed by one-way ANOVA (E, F, L, M and N).

Figure S4. RalB regulates PD-L1 transcription through NF-κB and STAT3

A. PD-L1 mRNA levels in B16F10-shCtrl and B16F10-shRalB cells measured by qPCR.

B. PD-L1 mRNA levels in B16F10-shCtrl and B16F10-shRalbp1 cells measured by qPCR.

C. PD-L1 mRNA levels in B16F10-shCtrl cells, B16F10-shRalB cells, and B16F10-shRalB cells reconstituted with wild-type RalB or the indicated mutants (G26A or C203S) measured by qPCR.
D. GSEA pathway analysis of RNA-seq data from RalB-knockdown B16F10 cells.
E. Immunoblot analysis of RalB, p-STAT1, STAT3, p-NFκB, NFκB, and GAPDH in total lysates from B16F10-shCtrl and B16F10-shRalB cells.
F. Stat3 and PD-L1 mRNA levels in B16F10-shCtrl and B16F10-shStat3 cells measured by qPCR.
G. PD-L1 mRNA levels in B16F10 cells treated with the Stat3 inhibitor Stattic (5 μM) measured by qPCR.
H. NFκB and PD-L1 mRNA levels in B16F10-shCtrl and B16F10-shNFκB cells measured by qPCR.
I. PD-L1 mRNA levels in B16F10 cells treated with the NFκB inhibitor BAY 11-7082 (2 μM) measured by qPCR.
J. PD-L1 mRNA levels in B16F10-shCtrl cells, B16F10 cells with dual knockdown of NFκB and Stat3, and B16F10 cells with triple knockdown of NFκB, Stat3, and RalB measured by qPCR.

Data are mean ± SD from three independent experiments. Statistical significance was assessed by Student's t-test (G and I), one-way ANOVA (A, B, C and J), or two-way ANOVA (F and H).

Figure 4. Inhibition of the RalB/Ralbp1 sensitizes tumor cells to CD8+ T cell cytotoxicity

A. Cytotoxicity assay of RalB-knockdown B16F10-OVA cells co-cultured with OT-1 CD8$^+$ T cells.
B. Cytotoxicity assay of RalB-knockdown MC38-OVA cells co-cultured with OT-1 CD8$^+$ T cells.
C. Cytotoxicity assay of Ralbp1-knockdown B16F10-OVA cells co-cultured with OT-1 CD8$^+$ T cells.
D. Cytotoxicity assay of Ralbp1-knockdown MC38-OVA cells co-cultured with OT-1 CD8$^+$ T cells.
E. Tumor growth curves of B16F10-shCtrl, B16F10-shRalB, and B16F10-shRalbp1 allografts in C57BL/6 mice.
F. Tumor weights of B16F10-shRalB and B16F10-shRalbp1 allografts in C57BL/6 mice at the experimental endpoint.
G. Percentage of intratumoral CD8$^+$ T cells among CD45$^+$ tumor-infiltrating leukocytes in B16F10-shCtrl, B16F10-shRalB, and B16F10-shRalbp1 tumors.
H. Quantification of GZMB$^+$ cells within the intratumoral CD8$^+$ T cell population in B16F10-shCtrl, B16F10-shRalB, and B16F10-shRalbp1 tumors.

Data are mean ± SD from three independent experiments or at least six mice per group. Statistical significance was assessed by one-way ANOVA (F, G and H) or two-way ANOVA (A, B, C, D and E).

Figure 5. Pharmacological inhibition of FDPS sensitizes tumor cells to immune checkpoint blockade

A. Images of the B16F10 tumors treated with risedronate, anti-PD-1, or risedronate plus anti-PD-1.

B. Tumor growth curves of B16F10 allografts in C57BL/6 mice treated with risedronate, anti–PD-1, or risedronate plus anti–PD-1.
C. Tumor weights of B16F10 allografts at the experimental endpoint in C57BL/6 mice treated with risedronate, anti–PD-1, or risedronate plus anti–PD-1.
D. Images of B16F10 tumors from C57BL/6 mice treated with zoledronate, anti–CTLA-4, or zoledronate plus anti–CTLA-4.
E. Tumor growth curves of B16F10 allografts in C57BL/6 mice treated with zoledronate, anti–CTLA-4, or zoledronate plus anti–CTLA-4.
F. Tumor weights of B16F10 allografts at the experimental endpoint in C57BL/6 mice treated with zoledronate, anti–CTLA-4, or zoledronate plus anti–CTLA-4.
G. H&E-stained tissue sections. Scale bar, 20 µm (heart, liver, kidney) or 50 µm (lung).
H. Body weight of tumor-bearing C57BL/6 mice treated with risedronate, anti–PD-1, or risedronate plus anti–PD-1.
I. Body weight of tumor-bearing C57BL/6 mice treated with zoledronate, anti–CTLA-4, or zoledronate plus anti–CTLA-4.
J. Percentage of intratumoral $CD8^+$ T cells among $CD45^+$ tumor-infiltrating leukocytes.

Data are mean ± SD from six mice per group. Statistical significance was assessed by one-way ANOVA (C, F and J) or two-way ANOVA (B, E and H).

Figure S5. The combination of nitrogen-containing bisphosphonates and immunotherapy exhibits no inflammatory response in vivo

A. Percentages of $CD4^+$ and $CD8^+$ T cells among $CD45^+$ cells in draining lymph nodes.
B. Percentages of $CD4^+$ and $CD8^+$ T cells among $CD45^+$ cells in spleen.
C. Percentages of macrophages, monocytes, neutrophils and dendritic cells among $CD45^+$ cells in draining lymph nodes.
D. Percentage of macrophages, monocytes, neutrophils and dendritic cells among $CD45^+$ cells in spleen.

Data are mean ± SD from six mice per group.

Figure 6. Clinical relevance of the FDPS-RalB-PD-L1 axis

(A-D) Cell-surface PD-L1 in human melanoma and colorectal cancer cell lines after FDPS knockdown, measured by flow cytometry. A375 (A), SK-MEL-103 (B), RKO (C), and HCT116 (D).

(E-H) Cell-surface PD-L1 in human melanoma and colorectal cancer cell lines after RalB knockdown, measured by flow cytometry. A375 (E), SK-MEL-103 (F), RKO (G), and HCT116 (H).

I. Schematic of the antigen-specific cytotoxicity coculture system using A375 cells engineered to express NY-ESO-1 and HLA-A2 (A375-A2-ESO) and PBMC-derived CD8$^+$ T cells engineered to express an NY-ESO-1–specific TCR.

J. Cytotoxicity assay of A375-A2-ESO tumor cells with FDPS or RalB knockdown co-cultured with PBMC-derived NY-ESO-1-specific TCR CD8$^+$ T cells.

K. Correlation analysis between FDPS expression and CD8$^+$ T cell infiltration in COAD and SKCM datasets using the Timer 2.0 platform.

L. Correlation analysis between RalB and CD274 expression in COAD and SKCM datasets using the Timer 2.0 platform.

M. Kaplan–Meier analysis of overall survival in SKCM stratified by tumor FDPS expression.

Data are mean ± SD from three independent experiments. Statistical significance was assessed by one-way ANOVA (A–J).

References

1. Wherry, E.J., T cell exhaustion. Nature immunology, 2011. **12**(6): p. 492-499.
2. Dyck, L. and K.H. Mills, Immune checkpoints and their inhibition in cancer and infectious diseases. European journal of immunology, 2017. **47**(5): p. 765-779.
3. Arner, E.N. and J.C. Rathmell, Metabolic programming and immune suppression in the tumor microenvironment. Cancer cell, 2023. **41**(3): p. 421-433.
4. Juarez, D. and D.A. Fruman, Targeting the mevalonate pathway in cancer. Trends in cancer, 2021. **7**(6): p. 525-540.
5. Hebert, P.R., et al., Cholesterol lowering with statin drugs, risk of stroke, and total mortality: an overview of randomized trials. Jama, 1997. **278**(4): p. 313-321.
6. Jain, M.K. and P.M. Ridker, Anti-inflammatory effects of statins: clinical evidence and basic mechanisms. Nature reviews Drug discovery, 2005. **4**(12): p. 977-987.
7. Vaughan, C.J., M.B. Murphy, and B.M. Buckley, Statins do more than just lower cholesterol. The Lancet, 1996. **348**(9034): p. 1079-1082.
8. Ma, X., et al., Cholesterol Induces CD8(+) T Cell Exhaustion in the Tumor Microenvironment. Cell Metab, 2019. **30**(1): p. 143-156.e5.
9. Wang, M. and P.J. Casey, Protein prenylation: unique fats make their mark on biology. Nat Rev Mol Cell Biol, 2016. **17**(2): p. 110-22.
10. Charron, G., et al., Alkynyl-farnesol reporters for detection of protein S-prenylation in cells. Mol Biosyst, 2011. **7**(1): p. 67-73.
11. Burr, M.L., et al., CMTM6 maintains the expression of PD-L1 and regulates anti-tumour immunity. Nature, 2017. **549**(7670): p. 101-105.
12. Chen, X., et al., A membrane-associated MHC-I inhibitory axis for cancer immune evasion. Cell, 2023. **186**(18): p. 3903-3920.e21.
13. Li, B., et al., Serotonin transporter inhibits antitumor immunity through regulating the intratumoral serotonin axis. Cell, 2025. **188**(14): p. 3823-3842.e21.
14. Thurnher, M. and G. Gruenbacher, T lymphocyte regulation by mevalonate metabolism. Sci Signal, 2015. **8**(370): p. re4.
15. Harly, C., et al., Key implication of CD277/butyrophilin-3 (BTN3A) in cellular stress sensing by a major human γδ T-cell subset. Blood, 2012. **120**(11): p. 2269-79.
16. Vavassori, S., et al., Butyrophilin 3A1 binds phosphorylated antigens and stimulates human γδ T cells. Nat Immunol, 2013. **14**(9): p. 908-16.
17. Yang, W., et al., Potentiating the antitumour response of CD8(+) T cells by modulating cholesterol metabolism. Nature, 2016. **531**(7596): p. 651-5.
18. Zhang, X., et al., Farnesyl pyrophosphate potentiates dendritic cell migration in autoimmunity through mitochondrial remodelling. Nat Metab, 2024. **6**(11): p. 2118-2137.
19. Lemma, E.Y., et al., Regulation of PD-L1 Trafficking from Synthesis to Degradation. Cancer Immunol Res, 2023. **11**(7): p. 866-874.

20. Zerdes, I., et al., Genetic, transcriptional and post-translational regulation of the programmed death protein ligand 1 in cancer: biology and clinical correlations. Oncogene, 2018. **37**(34): p. 4639-4661.
21. Chen, S., et al., Mechanisms regulating PD-L1 expression on tumor and immune cells. J Immunother Cancer, 2019. **7**(1): p. 305.
22. Yan, Y., et al., Interferon regulatory factor 1 (IRF-1) and IRF-2 regulate PD-L1 expression in hepatocellular carcinoma (HCC) cells. Cancer Immunol Immunother, 2020. **69**(9): p. 1891-1903.
23. Antonangeli, F., et al., Regulation of PD-L1 Expression by NF-κB in Cancer. Front Immunol, 2020. **11**: p. 584626.
24. Marzec, M., et al., Oncogenic kinase NPM/ALK induces through STAT3 expression of immunosuppressive protein CD274 (PD-L1, B7-H1). Proc Natl Acad Sci U S A, 2008. **105**(52): p. 20852-7.
25. Li, C.W., et al., Glycosylation and stabilization of programmed death ligand-1 suppresses T-cell activity. Nat Commun, 2016. **7**: p. 12632.
26. Letian, A., et al., Proximity proteome mapping reveals PD-L1-dependent pathways disrupted by anti-PD-L1 antibody specifically in EGFR-mutant lung cancer cells. Cell Commun Signal, 2023. **21**(1): p. 58.
27. Mezzadra, R., et al., Identification of CMTM6 and CMTM4 as PD-L1 protein regulators. Nature, 2017. **549**(7670): p. 106-110.
28. Ren, Y., et al., TRAPPC4 regulates the intracellular trafficking of PD-L1 and antitumor immunity. Nat Commun, 2021. **12**(1): p. 5405.
29. Wang, H., et al., HIP1R targets PD-L1 to lysosomal degradation to alter T cell-mediated cytotoxicity. Nat Chem Biol, 2019. **15**(1): p. 42-50.
30. Nielsen, S.F., B.G. Nordestgaard, and S.E. Bojesen, Statin use and reduced cancer-related mortality. N Engl J Med, 2013. **368**(6): p. 576-7.
31. Kubatka, P., et al., Statins in oncological research: from experimental studies to clinical practice. Crit Rev Oncol Hematol, 2014. **92**(3): p. 296-311.
32. Chae, Y.K., et al., Reduced risk of breast cancer recurrence in patients using ACE inhibitors, ARBs, and/or statins. Cancer Invest, 2011. **29**(9): p. 585-93.
33. Garwood, S., Statins and cardiac surgery. J Cardiothorac Vasc Anesth, 2010. **24**(6): p. 909-12.
34. Sanfilippo, K.M., et al., Statins Are Associated With Reduced Mortality in Multiple Myeloma. J Clin Oncol, 2016. **34**(33): p. 4008-4014.
35. Zhou, W., et al., Targeting the mevalonate pathway suppresses ARID1A-inactivated cancers by promoting pyroptosis. Cancer Cell, 2023. **41**(4): p. 740-756.e10.
36. Yang, J., et al., Administration of statins is correlated with favourable prognosis in lung cancer patients receiving immune checkpoint inhibitors. Front Immunol, 2025. **16**: p. 1638677.
37. Chen, Y., et al., Mevalonate pathway promotes liver cancer by suppressing ferroptosis through

CoQ10 production and selenocysteine-tRNA modification. J Hepatol, 2025. **83**(6): p. 1338-1352.

38. Okoye, I., et al., Atorvastatin downregulates co-inhibitory receptor expression by targeting Ras-activated mTOR signalling. Oncotarget, 2017. **8**(58): p. 98215-98232.
39. Reszka, A.A. and G.A. Rodan, Nitrogen-containing bisphosphonate mechanism of action. Mini Rev Med Chem, 2004. **4**(7): p. 711-9.
40. Xia, Y., et al., The Mevalonate Pathway Is a Druggable Target for Vaccine Adjuvant Discovery. Cell, 2018. **175**(4): p. 1059-1073.e21.
41. Hiraga, T., et al., The bisphosphonate ibandronate promotes apoptosis in MDA-MB-231 human breast cancer cells in bone metastases. Cancer Res, 2001. **61**(11): p. 4418-24.
42. Hurst, M. and S. Noble, Clodronate: a review of its use in breast cancer. Drugs Aging, 1999. **15**(2): p. 143-67.
43. Hortobagyi, G.N., et al., Efficacy of pamidronate in reducing skeletal complications in patients with breast cancer and lytic bone metastases. Protocol 19 Aredia Breast Cancer Study Group. N Engl J Med, 1996. **335**(24): p. 1785-91.
44. Reszka, A.A., et al., Bisphosphonates act directly on the osteoclast to induce caspase cleavage of mst1 kinase during apoptosis. A link between inhibition of the mevalonate pathway and regulation of an apoptosis-promoting kinase. J Biol Chem, 1999. **274**(49): p. 34967-73.
45. Sasaki, A., et al., Bisphosphonate risedronate reduces metastatic human breast cancer burden in bone in nude mice. Cancer Res, 1995. **55**(16): p. 3551-7.
46. Singh, T., et al., The critical role of bisphosphonates to target bone cancer metastasis: an overview. J Drug Target, 2015. **23**(1): p. 1-15.

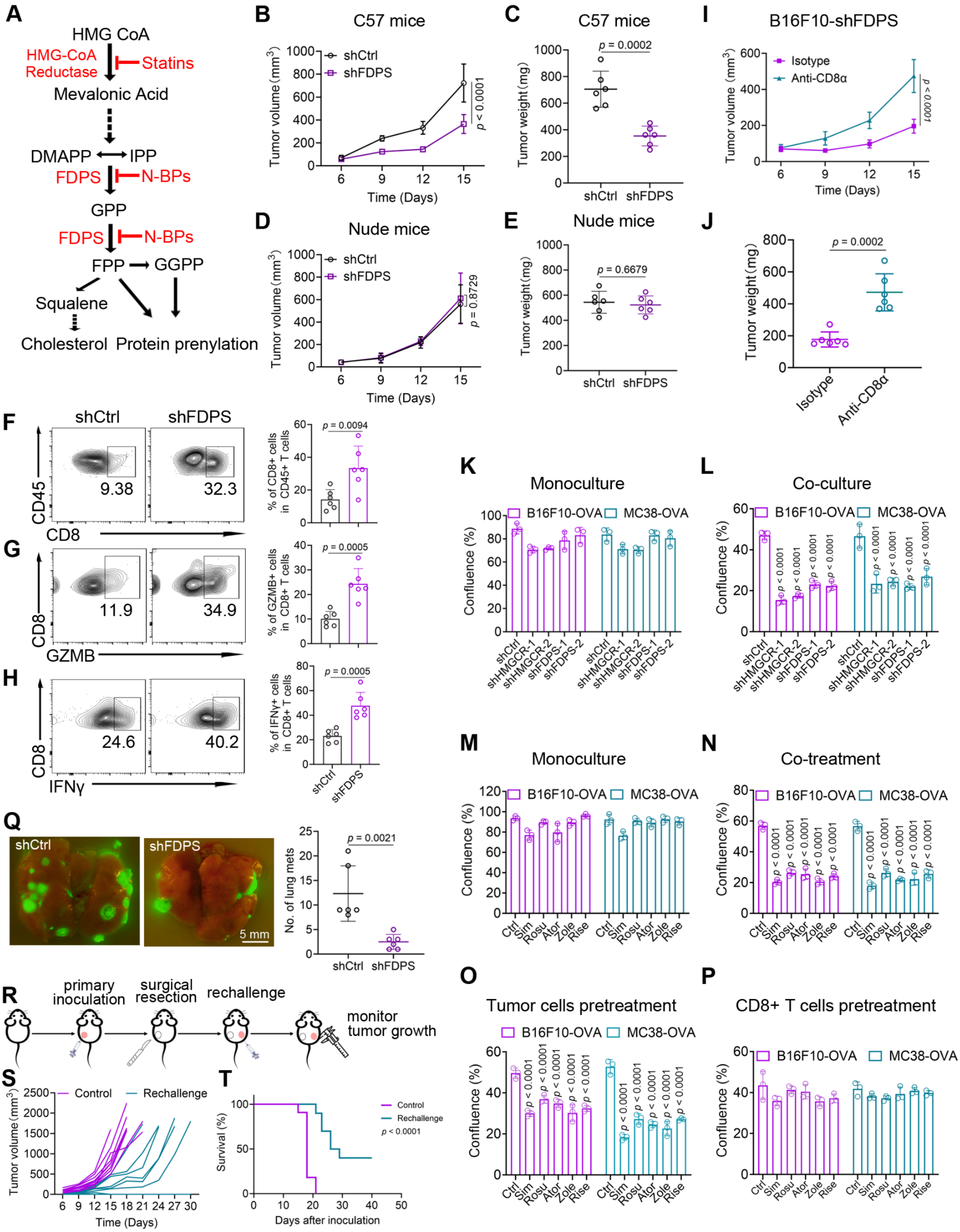
A
HMG CoA
HMG-CoA Reductase
Statins
Mevalonic Acid
DMAPP
IPP
FDPS
N-BPs
GPP
FDPS
N-BPs
FPP
GGPP
Squalene
Cholesterol
Protein prenylation
B
C57 mice
shCtrl
shFDPS
Tumor volume (mm³)
Time (Days)
p < 0.0001
C
C57 mice
p = 0.0002
Tumor weight (mg)
shCtrl
shFDPS
I
B16F10-shFDPS
Isotype
Anti-CD8α
Tumor volume (mm³)
Time (Days)
p < 0.0001
D
Nude mice
shCtrl
shFDPS
Tumor volume (mm³)
Time (Days)
p = 0.8729
E
Nude mice
p = 0.6679
Tumor weight (mg)
shCtrl
shFDPS
J
p = 0.0002
Tumor weight (mg)
Isotype
Anti-CD8α
F
shCtrl
shFDPS
CD45
CD8
9.38
32.3
p = 0.0094
% of CD8+ cells in CD45+ T cells
G
CD8
GZMB
11.9
34.9
p = 0.0005
% of GZMB+ cells in CD8+ T cells
H
CD8
IFNγ
24.6
40.2
p = 0.0005
% of IFNγ+ cells in CD8+ T cells
shCtrl
shFDPS
K
Monoculture
B16F10-OVA
MC38-OVA
Confluence (%)
shCtrl
shHMGCR-1
shHMGCR-2
shFDPS-1
shFDPS-2
L
Co-culture
B16F10-OVA
MC38-OVA
Confluence (%)
p < 0.0001
shCtrl
shHMGCR-1
shHMGCR-2
shFDPS-1
shFDPS-2
M
Monoculture
B16F10-OVA
MC38-OVA
Confluence (%)
Ctrl
Sim
Rosu
Ator
Zole
Rise
N
Co-treatment
B16F10-OVA
MC38-OVA
Confluence (%)
p < 0.0001
Ctrl
Sim
Rosu
Ator
Zole
Rise
Q
shCtrl
shFDPS
5 mm
p = 0.0021
No. of lung mets
shCtrl
shFDPS
R
primary inoculation
surgical resection
rechallenge
monitor tumor growth
S
Control
Rechallenge
Tumor volume (mm³)
Time (Days)
T
Control
Rechallenge
p < 0.0001
Survival (%)
Days after inoculation
O
Tumor cells pretreatment
B16F10-OVA
MC38-OVA
Confluence (%)
p < 0.0001
Ctrl
Sim
Rosu
Ator
Zole
Rise
P
CD8+ T cells pretreatment
B16F10-OVA
MC38-OVA
Confluence (%)
Ctrl
Sim
Rosu
Ator
Zole
Rise

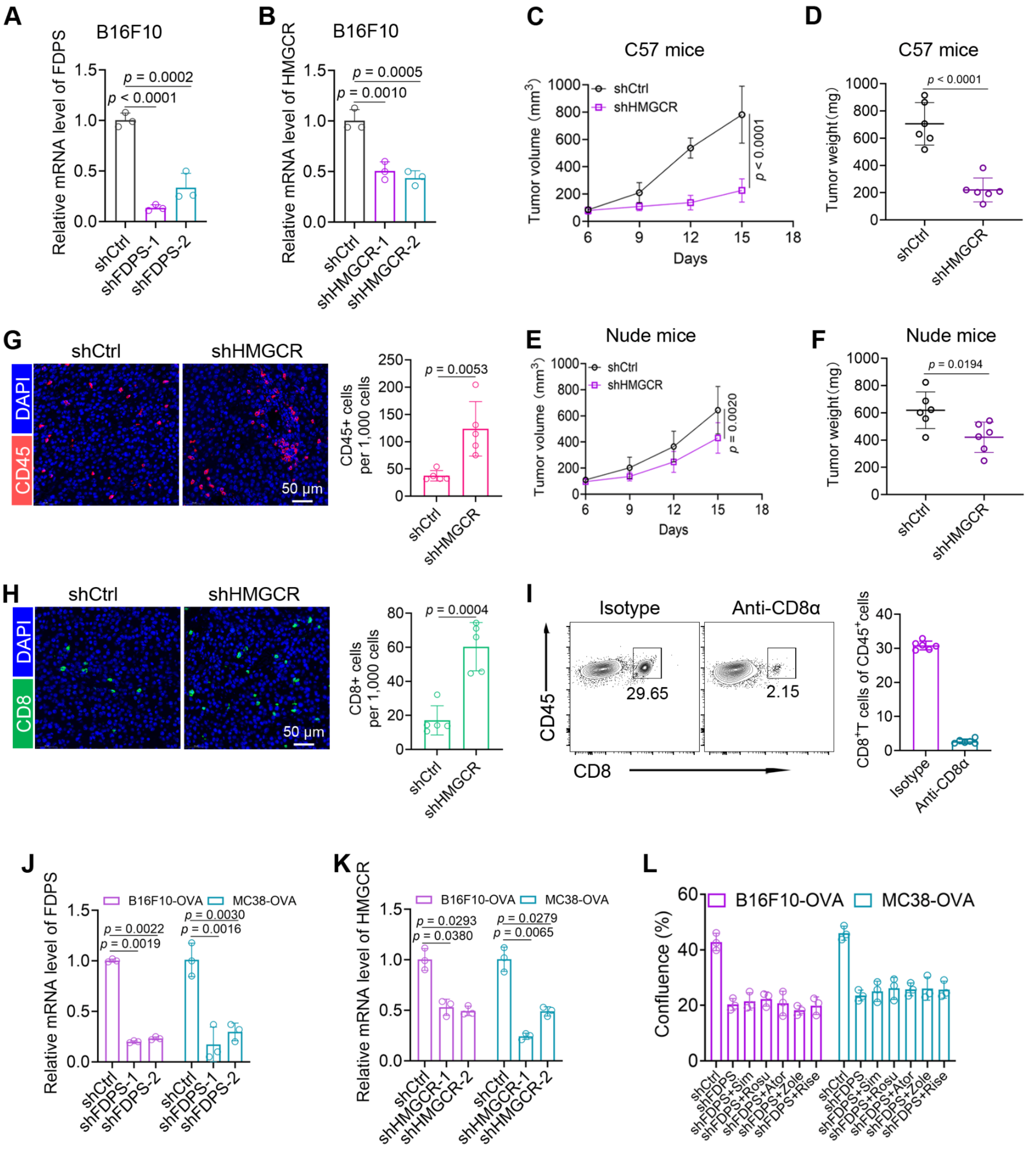
A
B16F10
Relative mRNA level of FDPS
p = 0.0002
p < 0.0001
shCtrl
shFDPS-1
shFDPS-2
B
B16F10
Relative mRNA level of HMGCR
p = 0.0005
p = 0.0010
shCtrl
shHMGCR-1
shHMGCR-2
C
C57 mice
Tumor volume (mm3)
shCtrl
shHMGCR
p < 0.0001
Days
D
C57 mice
Tumor weight (mg)
p < 0.0001
shCtrl
shHMGCR
G
shCtrl
shHMGCR
DAPI
CD45
50 μm
CD45+ cells per 1,000 cells
p = 0.0053
shCtrl
shHMGCR
E
Nude mice
Tumor volume (mm3)
shCtrl
shHMGCR
p = 0.0020
Days
F
Nude mice
Tumor weight (mg)
p = 0.0194
shCtrl
shHMGCR
H
shCtrl
shHMGCR
DAPI
CD8
50 μm
CD8+ cells per 1,000 cells
p = 0.0004
shCtrl
shHMGCR
I
Isotype
Anti-CD8α
CD45
CD8
29.65
2.15
CD8+T cells of CD45+cells
Isotype
Anti-CD8α
J
B16F10-OVA
MC38-OVA
Relative mRNA level of FDPS
p = 0.0022
p = 0.0019
p = 0.0030
p = 0.0016
shCtrl
shFDPS-1
shFDPS-2
K
B16F10-OVA
MC38-OVA
Relative mRNA level of HMGCR
p = 0.0293
p = 0.0380
p = 0.0279
p = 0.0065
shCtrl
shHMGCR-1
shHMGCR-2
L
B16F10-OVA
MC38-OVA
Confluence (%)
shCtrl
shFDPS
shFDPS+Sim
shFDPS+Rosu
shFDPS+Ator
shFDPS+Zole
shFDPS+Rise

control CD8+ T cells function

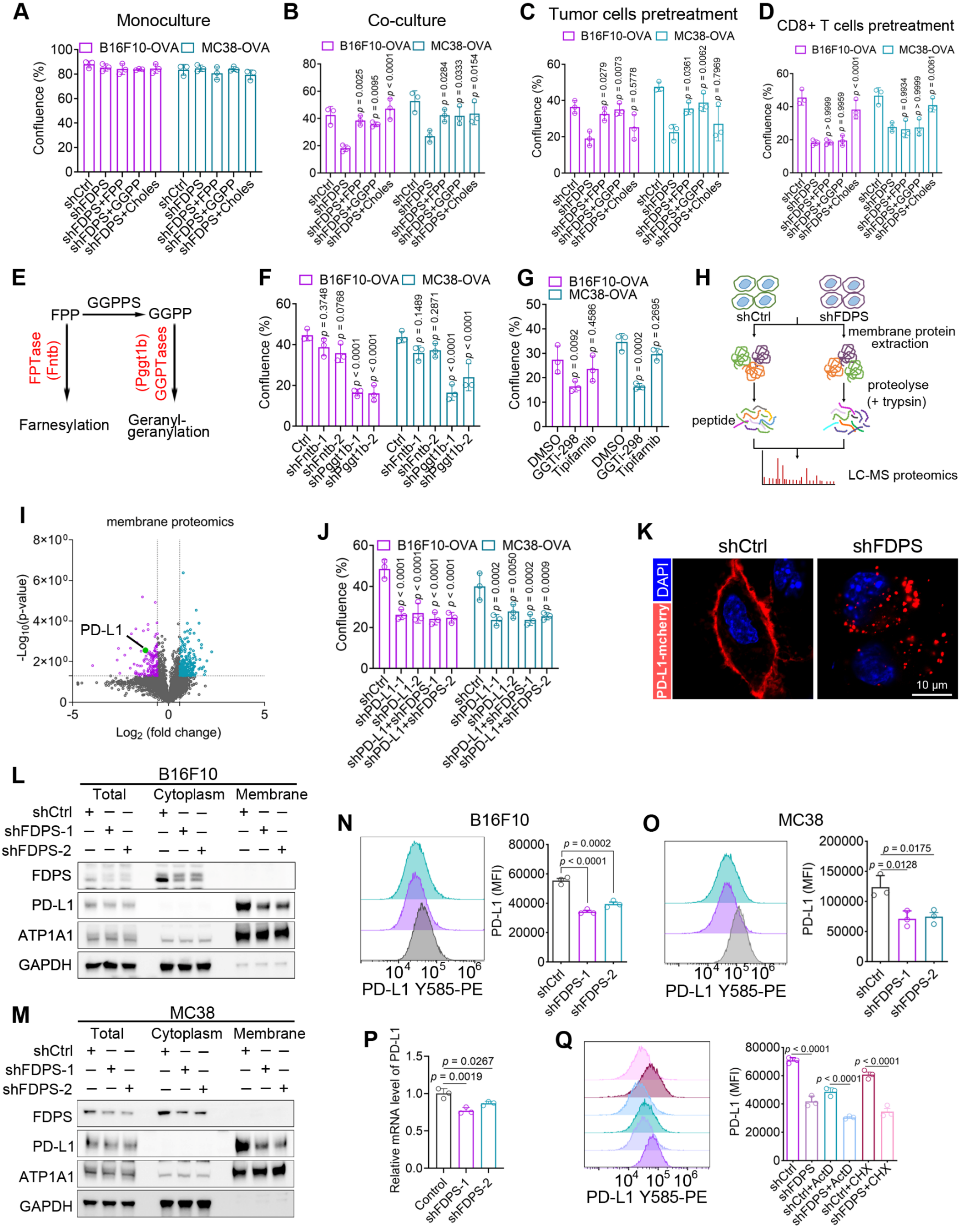

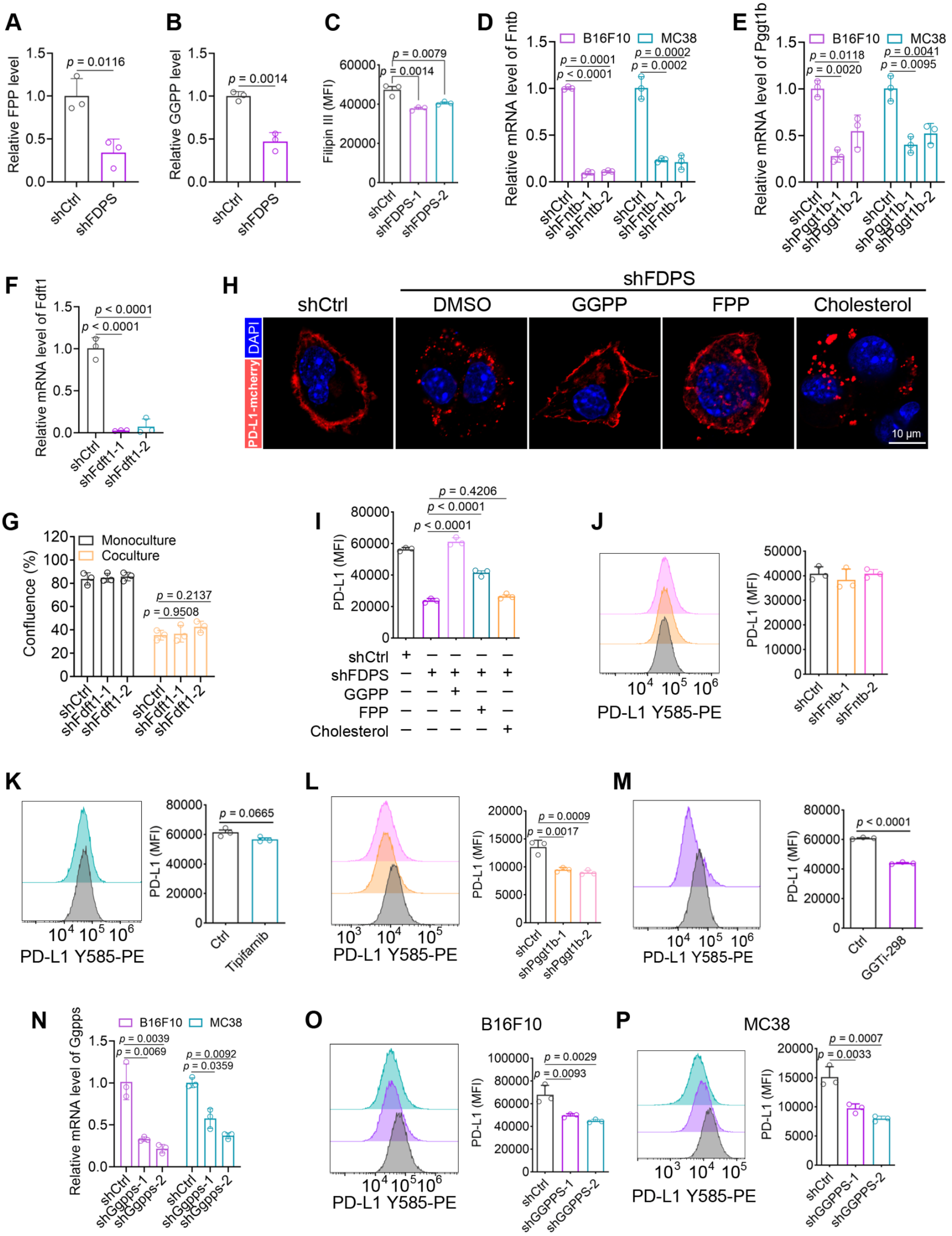
A
Relative FPP level
p = 0.0116
shCtrl
shFDPS
B
Relative GGPP level
p = 0.0014
shCtrl
shFDPS
C
Filipin III (MFI)
p = 0.0079
p = 0.0014
shCtrl
shFDPS-1
shFDPS-2
D
Relative mRNA level of Fntb
B16F10
MC38
p = 0.0001
p < 0.0001
p = 0.0002
p = 0.0002
shCtrl
shFntb-1
shFntb-2
E
Relative mRNA level of Pggt1b
B16F10
MC38
p = 0.0118
p = 0.0020
p = 0.0041
p = 0.0095
shCtrl
shPggt1b-1
shPggt1b-2
F
Relative mRNA level of Fdft1
p < 0.0001
p < 0.0001
shCtrl
shFdft1-1
shFdft1-2
H
shFDPS
shCtrl
DMSO
GGPP
FPP
Cholesterol
DAPI
PD-L1-mcherry
10 μm
G
Confluence (%)
Monoculture
Coculture
p = 0.2137
p = 0.9508
shCtrl
shFdft1-1
shFdft1-2
I
PD-L1 (MFI)
p = 0.4206
p < 0.0001
p < 0.0001
shCtrl + − − − −
shFDPS − + + + +
GGPP − − + − −
FPP − − − + −
Cholesterol − − − − +
J
PD-L1 Y585-PE
PD-L1 (MFI)
shCtrl
shFntb-1
shFntb-2
K
PD-L1 Y585-PE
PD-L1 (MFI)
p = 0.0665
Ctrl
Tipifarnib
L
PD-L1 Y585-PE
PD-L1 (MFI)
p = 0.0009
p = 0.0017
shCtrl
shPggt1b-1
shPggt1b-2
M
PD-L1 Y585-PE
PD-L1 (MFI)
p < 0.0001
Ctrl
GGTi-298
N
Relative mRNA level of Ggpps
B16F10
MC38
p = 0.0039
p = 0.0069
p = 0.0092
p = 0.0359
shCtrl
shGgpps-1
shGgpps-2
O
B16F10
PD-L1 Y585-PE
PD-L1 (MFI)
p = 0.0029
p = 0.0093
shCtrl
shGGPPS-1
shGGPPS-2
P
MC38
PD-L1 Y585-PE
PD-L1 (MFI)
p = 0.0007
p = 0.0033
shCtrl
shGGPPS-1
shGGPPS-2

activity

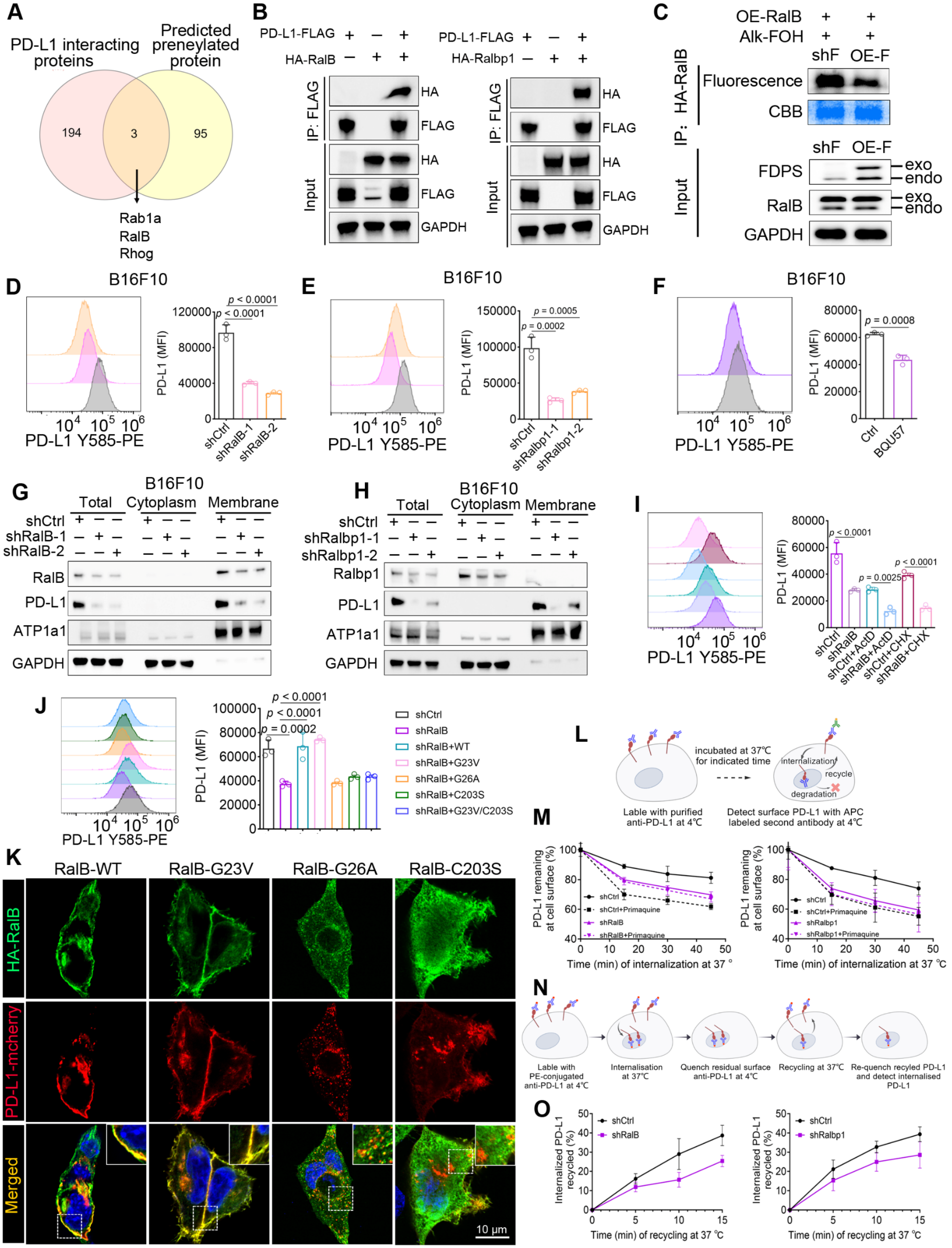
A
PD-L1 interacting proteins
Predicted preneylated protein
194
3
95
Rab1a
RalB
Rhog
B
PD-L1-FLAG + – +
HA-RalB – + +
IP: FLAG
HA
FLAG
Input
HA
FLAG
GAPDH
PD-L1-FLAG + – +
HA-Ralbp1 – + +
C
OE-RalB + +
Alk-FOH + +
shF OE-F
IP: HA-RalB
Fluorescence
CBB
Input
FDPS
RalB
GAPDH
exo
endo
D
B16F10
PD-L1 Y585-PE
PD-L1 (MFI)
p < 0.0001
shCtrl
shRalB-1
shRalB-2
E
p = 0.0005
p = 0.0002
shRalbp1-1
shRalbp1-2
F
p = 0.0008
Ctrl
BQU57
G
Total
Cytoplasm
Membrane
shCtrl
shRalB-1
shRalB-2
RalB
PD-L1
ATP1a1
GAPDH
H
shRalbp1-1
shRalbp1-2
Ralbp1
I
p = 0.0025
shRalB
shCtrl+ActD
shRalB+ActD
shCtrl+CHX
shRalB+CHX
J
p = 0.0002
shRalB+WT
shRalB+G23V
shRalB+G26A
shRalB+C203S
shRalB+G23V/C203S
K
RalB-WT
RalB-G23V
RalB-G26A
RalB-C203S
HA-RalB
PD-L1-mcherry
Merged
10 μm
L
Lable with purified anti-PD-L1 at 4℃
incubated at 37℃ for indicated time
internalization
recycle
degradation
Detect surface PD-L1 with APC labeled second antibody at 4℃
M
PD-L1 remaning at cell surface (%)
shCtrl
shCtrl+Primaquine
shRalB
shRalB+Primaquine
Time (min) of internalization at 37 °
shRalbp1
shRalbp1+Primaquine
Time (min) of internalization at 37 ℃
N
Lable with PE-conjugated anti-PD-L1 at 4℃
Internalisation at 37℃
Quench residual surface anti-PD-L1 at 4℃
Recycling at 37℃
Re-quench recycled PD-L1 and detect internalised PD-L1
O
Internalized PD-L1 recycled (%)
Time (min) of recycling at 37 ℃

activity

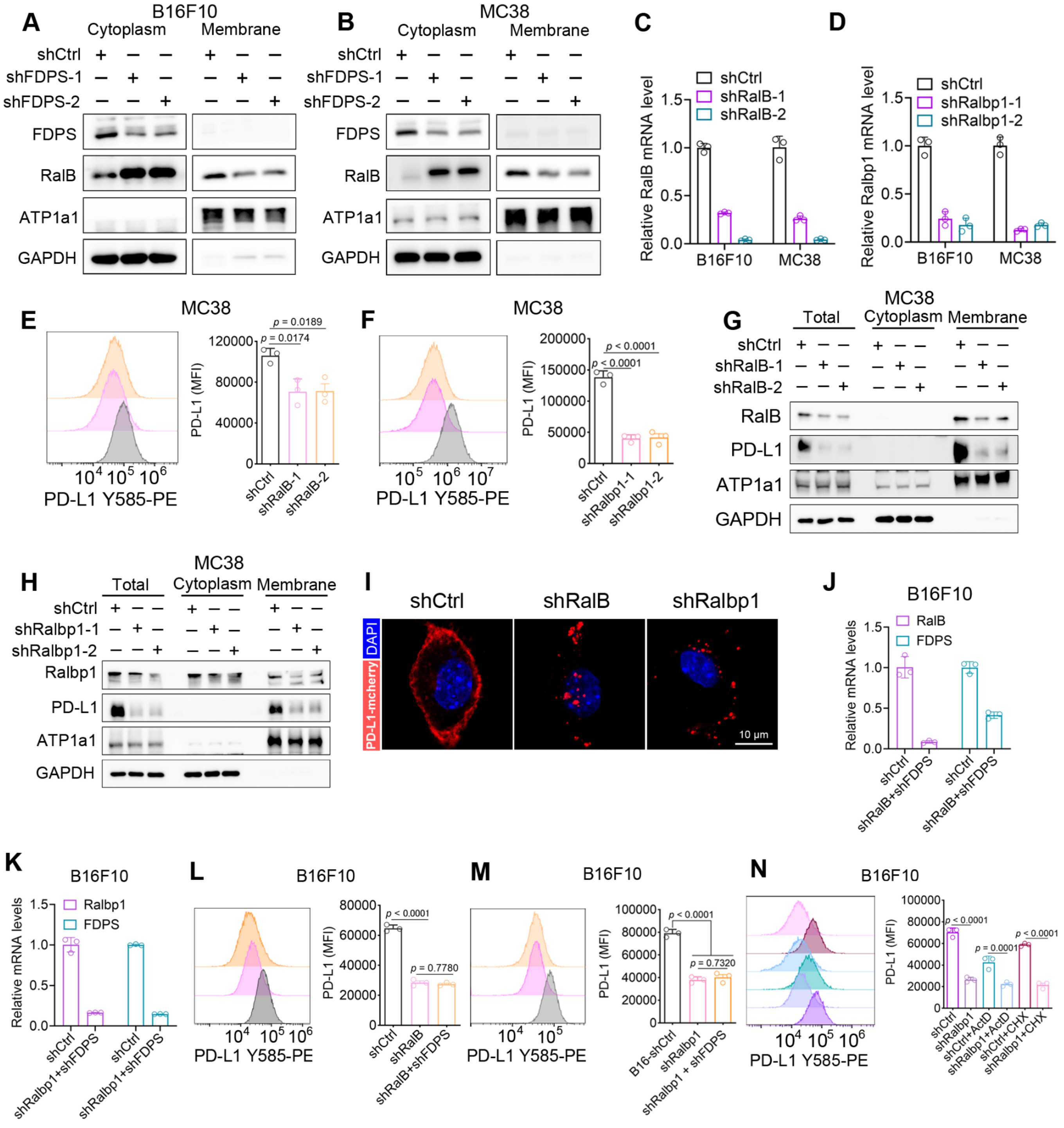
A
B16F10
Cytoplasm
Membrane
shCtrl
shFDPS-1
shFDPS-2
FDPS
RalB
ATP1a1
GAPDH
B
MC38
Cytoplasm
Membrane
shCtrl
shFDPS-1
shFDPS-2
FDPS
RalB
ATP1a1
GAPDH
C
Relative RalB mRNA level
shCtrl
shRalB-1
shRalB-2
B16F10
MC38
D
Relative Ralbp1 mRNA level
shCtrl
shRalbp1-1
shRalbp1-2
B16F10
MC38
E
MC38
PD-L1 Y585-PE
PD-L1 (MFI)
p = 0.0189
p = 0.0174
shCtrl
shRalB-1
shRalB-2
F
MC38
PD-L1 Y585-PE
PD-L1 (MFI)
p < 0.0001
p < 0.0001
shCtrl
shRalbp1-1
shRalbp1-2
G
MC38
Total
Cytoplasm
Membrane
shCtrl
shRalB-1
shRalB-2
RalB
PD-L1
ATP1a1
GAPDH
H
MC38
Total
Cytoplasm
Membrane
shCtrl
shRalbp1-1
shRalbp1-2
Ralbp1
PD-L1
ATP1a1
GAPDH
I
shCtrl
shRalB
shRalbp1
DAPI
PD-L1-mcherry
10 μm
J
B16F10
Relative mRNA levels
RalB
FDPS
shCtrl
shRalB+shFDPS
K
B16F10
Relative mRNA levels
Ralbp1
FDPS
shCtrl
shRalbp1+shFDPS
L
B16F10
PD-L1 Y585-PE
PD-L1 (MFI)
p < 0.0001
p = 0.7780
shCtrl
shRalB
shRalB+shFDPS
M
B16F10
PD-L1 Y585-PE
PD-L1 (MFI)
p < 0.0001
p = 0.7320
B16-shCtrl
shRalbp1
shRalbp1 + shFDPS
N
B16F10
PD-L1 Y585-PE
PD-L1 (MFI)
p < 0.0001
p = 0.0001
p < 0.0001
shCtrl
shRalbp1
shCtrl+ActD
shRalbp1+ActD
shCtrl+CHX
shRalbp1+CHX

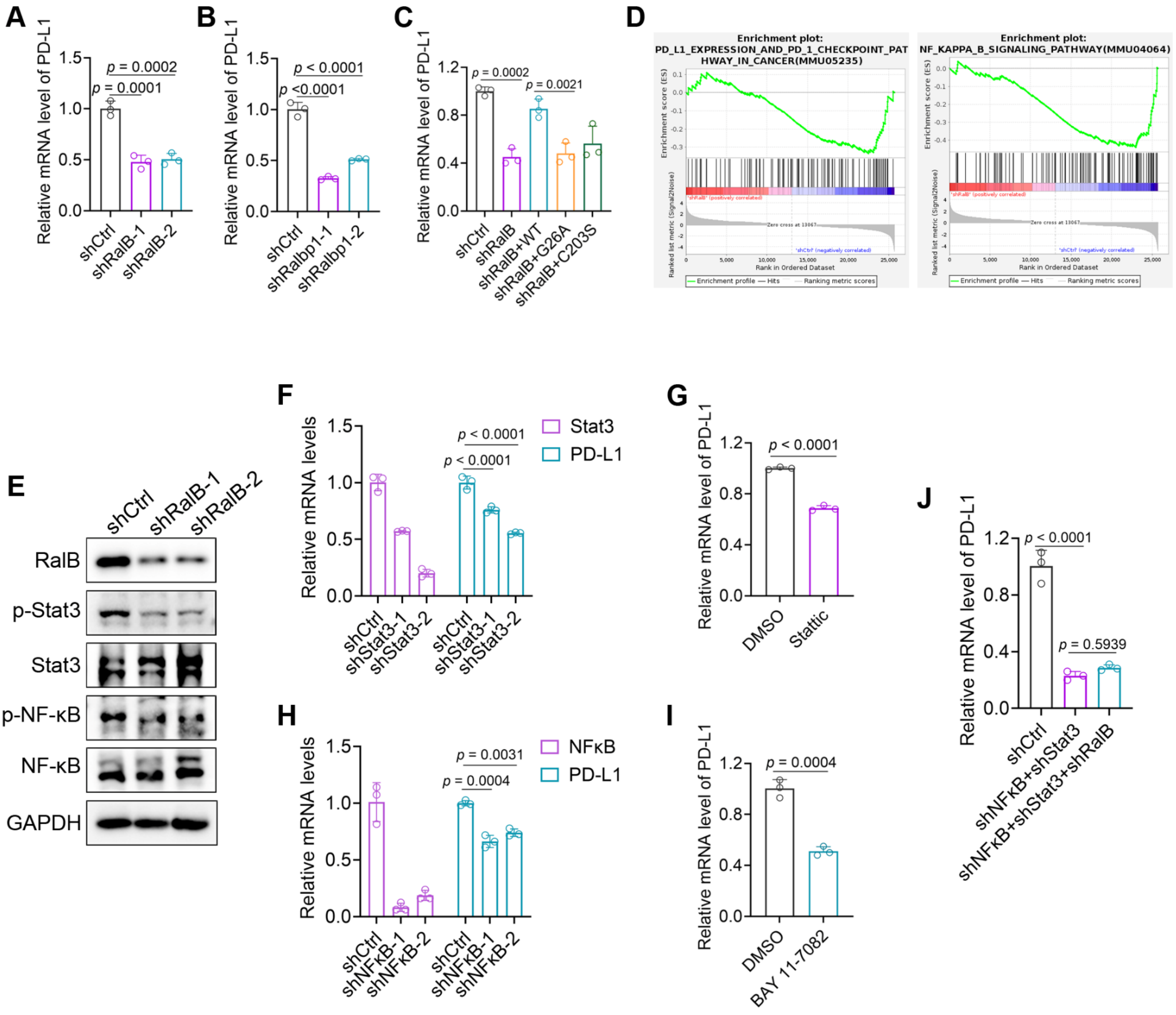
A
Relative mRNA level of PD-L1
p = 0.0002
p = 0.0001
shCtrl
shRalB-1
shRalB-2
B
Relative mRNA level of PD-L1
p < 0.0001
p <0.0001
shCtrl
shRalbp1-1
shRalbp1-2
C
Relative mRNA level of PD-L1
p = 0.0002
p = 0.0021
shCtrl
shRalB
shRalB+WT
shRalB+G26A
shRalB+C203S
D
Enrichment plot: PD_L1_EXPRESSION_AND_PD_1_CHECKPOINT_PATHWAY_IN_CANCER(MMU05235)
Enrichment plot: NF_KAPPA_B_SIGNALING_PATHWAY(MMU04064)
Enrichment score (ES)
Ranked list metric (Signal2Noise)
Rank in Ordered Dataset
'shRalB' (positively correlated)
'shCtrl' (negatively correlated)
Zero cross at 13067
Enrichment profile — Hits — Ranking metric scores
E
shCtrl
shRalB-1
shRalB-2
RalB
p-Stat3
Stat3
p-NF-κB
NF-κB
GAPDH
F
Relative mRNA levels
Stat3
PD-L1
p < 0.0001
p < 0.0001
shCtrl
shStat3-1
shStat3-2
G
Relative mRNA level of PD-L1
p < 0.0001
DMSO
Stattic
H
Relative mRNA levels
NFκB
PD-L1
p = 0.0031
p = 0.0004
shCtrl
shNFκB-1
shNFκB-2
I
Relative mRNA level of PD-L1
p = 0.0004
DMSO
BAY 11-7082
J
Relative mRNA level of PD-L1
p < 0.0001
p = 0.5939
shCtrl
shNFκB+shStat3
shNFκB+shStat3+shRalB

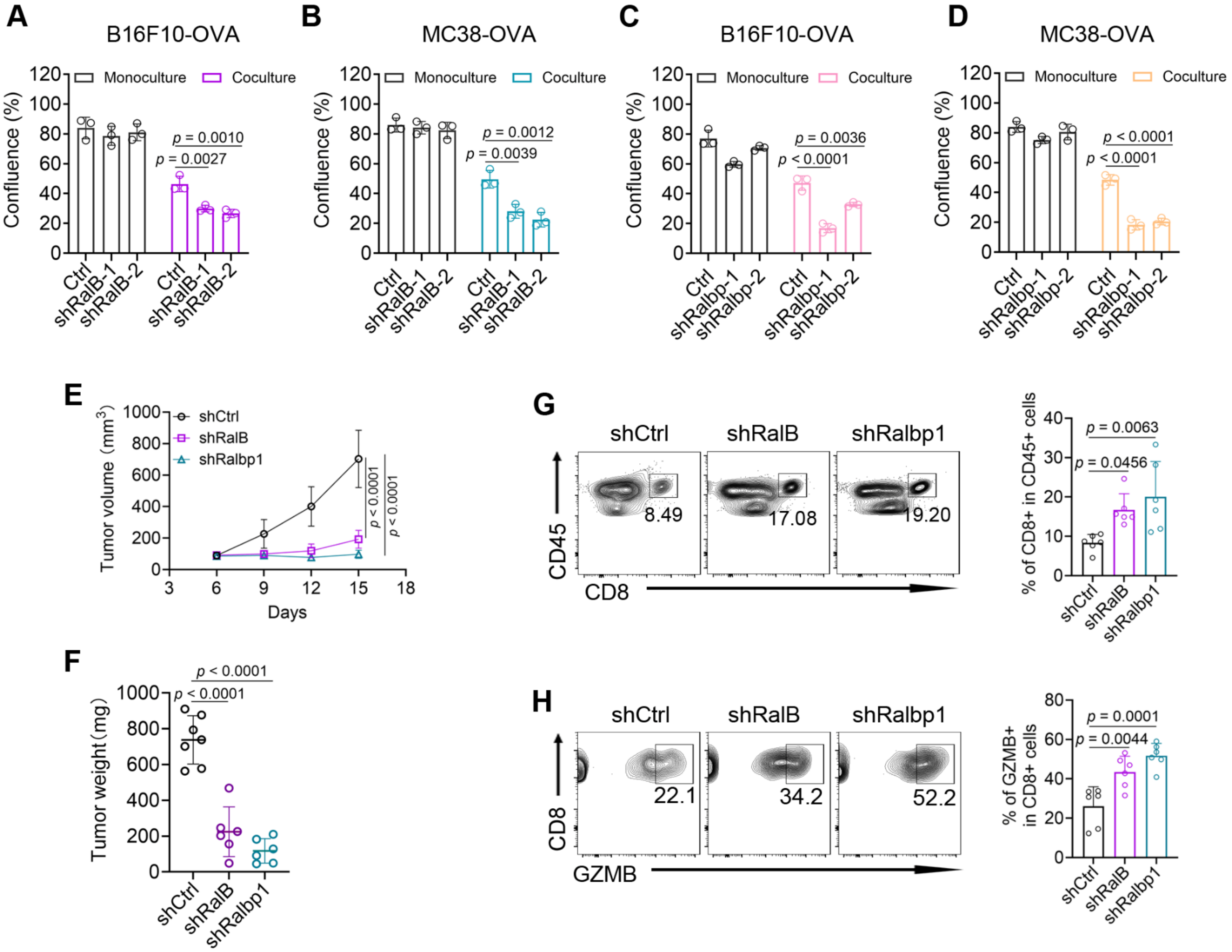
A
B16F10-OVA
Confluence (%)
Monoculture
Coculture
p = 0.0010
p = 0.0027
Ctrl
shRalB-1
shRalB-2
B
MC38-OVA
p = 0.0012
p = 0.0039
C
B16F10-OVA
p = 0.0036
p < 0.0001
shRalbp-1
shRalbp-2
D
MC38-OVA
p < 0.0001
p < 0.0001
E
Tumor volume (mm³)
shCtrl
shRalB
shRalbp1
p < 0.0001
p < 0.0001
Days
F
Tumor weight (mg)
p < 0.0001
p < 0.0001
G
CD45
CD8
8.49
17.08
19.20
% of CD8+ in CD45+ cells
p = 0.0063
p = 0.0456
H
GZMB
22.1
34.2
52.2
% of GZMB+ in CD8+ cells
p = 0.0001
p = 0.0044

blockade

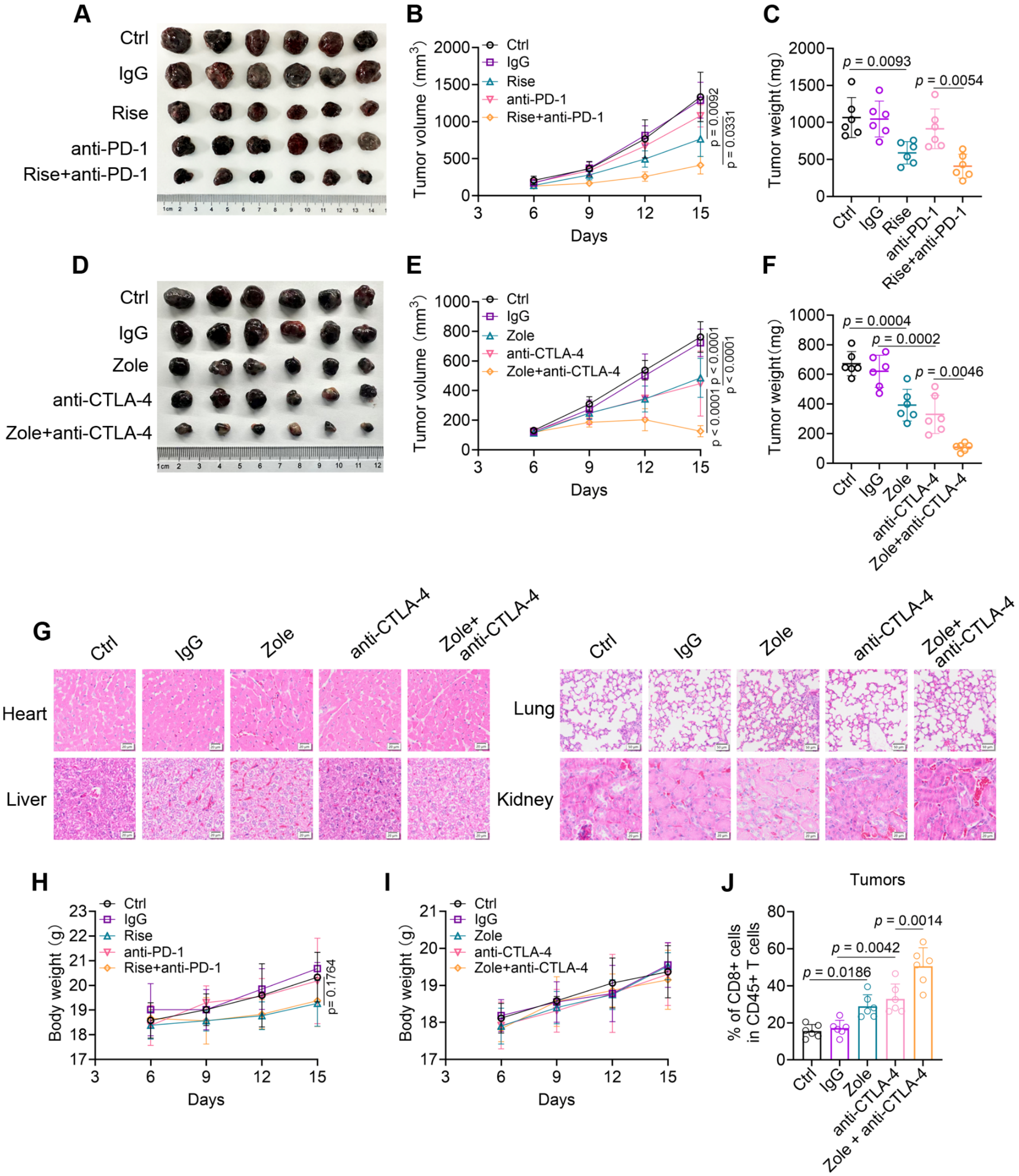
A
Ctrl
IgG
Rise
anti-PD-1
Rise+anti-PD-1
B
Tumor volume（mm³）
Days
Ctrl
IgG
Rise
anti-PD-1
Rise+anti-PD-1
p = 0.0092
p = 0.0331
C
Tumor weight (mg)
p = 0.0093
p = 0.0054
Ctrl
IgG
Rise
anti-PD-1
Rise+anti-PD-1
D
Ctrl
IgG
Zole
anti-CTLA-4
Zole+anti-CTLA-4
E
Tumor volume（mm³）
Days
Ctrl
IgG
Zole
anti-CTLA-4
Zole+anti-CTLA-4
p < 0.0001
p < 0.0001
p < 0.0001
F
Tumor weight (mg)
p = 0.0004
p = 0.0002
p = 0.0046
Ctrl
IgG
Zole
anti-CTLA-4
Zole+anti-CTLA-4
G
Ctrl
IgG
Zole
anti-CTLA-4
Zole+ anti-CTLA-4
Heart
Liver
Lung
Kidney
H
Body weight（g）
Days
Ctrl
IgG
Rise
anti-PD-1
Rise+anti-PD-1
p= 0.1764
I
Body weight（g）
Days
Ctrl
IgG
Zole
anti-CTLA-4
Zole+anti-CTLA-4
J
Tumors
% of CD8+ cells in CD45+ T cells
p = 0.0186
p = 0.0042
p = 0.0014
Ctrl
IgG
Zole
anti-CTLA-4
Zole + anti-CTLA-4

immunotherapy exhibits no significant toxicity in vivo

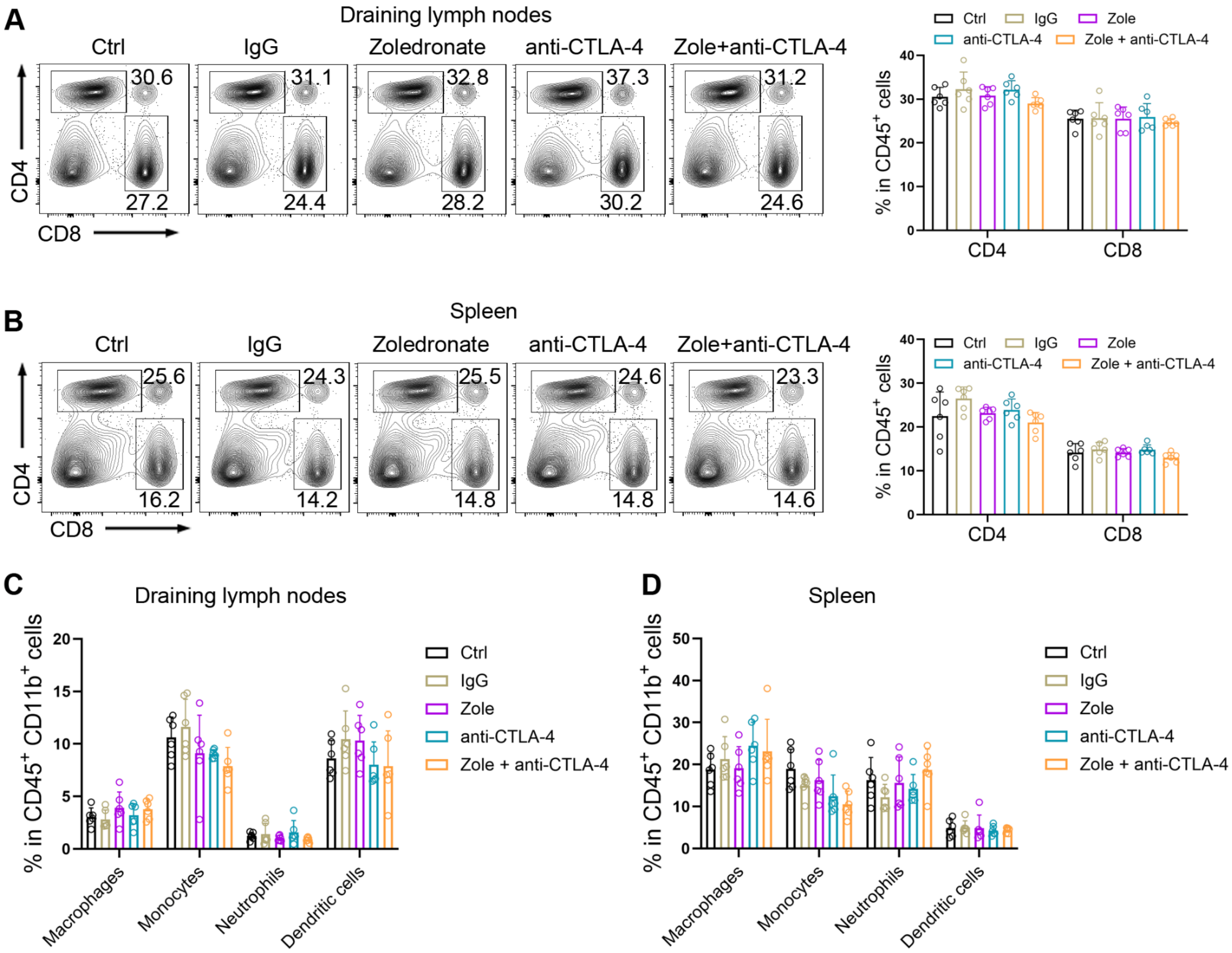

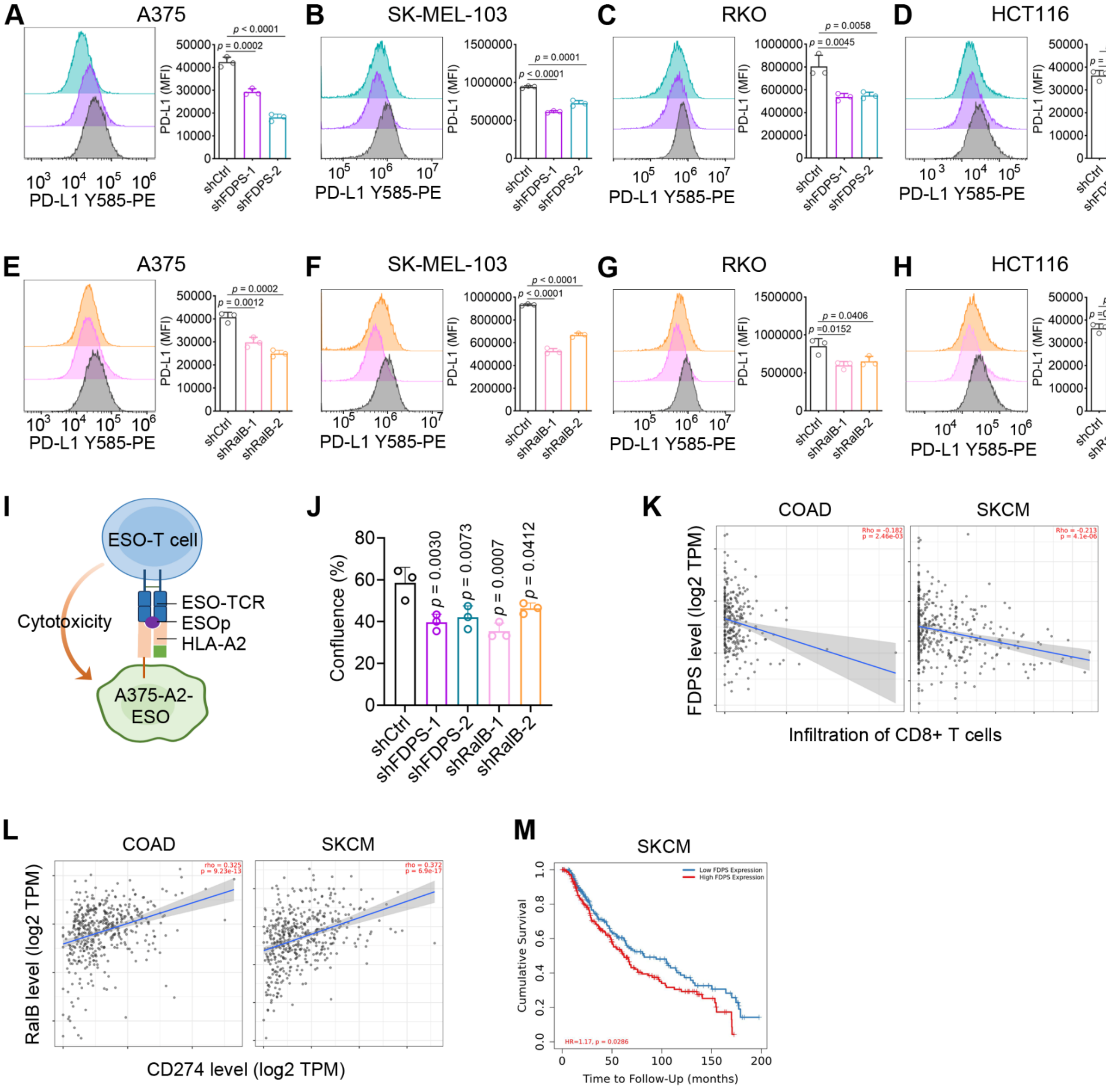
A
A375
p < 0.0001
p = 0.0002
PD-L1 (MFI)
PD-L1 Y585-PE
shCtrl
shFDPS-1
shFDPS-2
B
SK-MEL-103
p = 0.0001
p < 0.0001
C
RKO
p = 0.0058
p = 0.0045
D
HCT116
p = 0.0012
p = 0.0008
E
A375
p = 0.0002
p = 0.0012
shRalB-1
shRalB-2
F
SK-MEL-103
p < 0.0001
p < 0.0001
G
RKO
p = 0.0406
p = 0.0152
H
HCT116
p = 0.0002
p = 0.0004
I
ESO-T cell
Cytotoxicity
ESO-TCR
ESOp
HLA-A2
A375-A2-ESO
J
Confluence (%)
p = 0.0030
p = 0.0073
p = 0.0007
p = 0.0412
K
COAD
SKCM
Rho = -0.182
p = 2.46e-03
Rho = -0.213
p = 4.1e-06
FDPS level (log2 TPM)
Infiltration of CD8+ T cells
L
COAD
SKCM
rho = 0.325
p = 9.23e-13
rho = 0.372
p = 6.9e-17
RalB level (log2 TPM)
CD274 level (log2 TPM)
M
SKCM
Low FDPS Expression
High FDPS Expression
Cumulative Survival
HR=1.17, p = 0.0286
Time to Follow-Up (months)